J. Fluid Mech. (2000), *vol.* 412, *pp.* 227–257. Printed in the United Kingdom

Cusp formation for time-evolving bubbles in two-dimensional Stokes flow

By MICHAEL SIEGEL

Department of Mathematical Sciences, New Jersey Institute of Technology, Newark, NJ 07102, USA

(Received 12 August 1999)

Analytical and numerical methods are applied to investigate the transient evolution of an inviscid bubble in two-dimensional Stokes flow. The evolution is driven by extensional incident flow with a rotational component, such as occurs for flow in a four-roller mill. Of particular interest is the possible spontaneous occurrence of a cusp singularity on the bubble surface. The role of constant as well as variable surface tension, induced by the presence of surfactant, is considered. A general theory of time-dependent evolution, which includes the existence of a broad class of exact solutions, is presented. For constant surface tension, a conjecture concerning the existence of a critical capillary number above which all symmetric steady bubble solutions are linearly unstable is found to be false. Steady bubbles for large capillary number Q are found to be susceptible to finite-amplitude instability, with the dynamics often leading to cusp or topological singularities. The evolution of an initially circular bubble at zero surface tension is found to culminate in unsteady cusp formation. In contrast to the clean flow problem, for variable surface tension there exists an upper bound Q_c for which steady bubble solutions exist. Theoretical considerations as well as numerical calculations for $Q > Q_c$ verify that the bubble achieves an unsteady cusped formation in finite time. The role of a nonlinear equation of state and the influence of surface diffusion of surfactant are both considered. A possible connection between the observed behaviour and the phenomenon of tip streaming is discussed.

1. Introduction

Interest in the possible spontaneous occurrence of singularities on free surfaces in Stokes flow stems from experimental observations of the development of apparent corners or cusps in several classes of flows. The corners or cusps may appear briefly during time-dependent evolution, or persist in a steady state. Joseph (1992) and Pozrikidis (1997) review some of the flows where corner and cusp development are known or are expected to occur.

The pioneering experiments of G. I. Taylor were among the first to exhibit cusp formation on free surfaces in low Reynolds number flow. Taylor (1934) filled a four-roller mill (figure 1) with a highly viscous fluid and rotated the rollers in the directions shown, producing a strain flow in the neighbourhood of a drop or bubble at the centre of the mill. He then measured the dependence of steady drop deformation on a non-dimensional strain parameter $Q = 2\mu GR/\sigma_0$, where μ is the viscosity of the outer fluid, G is a parameter characterizing the strain rate far from the drop (G is related to the rotation rate of the rollers), and R is the undeformed drop radius. The most interesting behaviour occurred when the drop viscosity was much less than

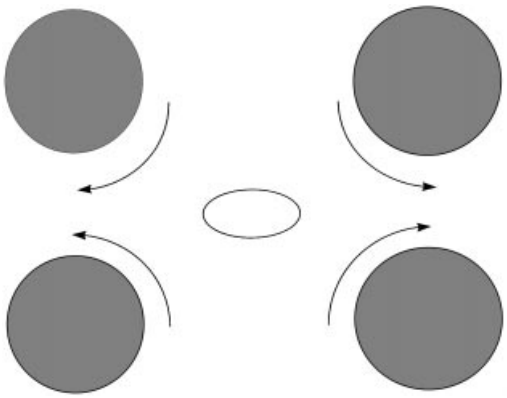

FIGURE 1. Taylor's four-roller mill. The four cylindrical rollers are rotated in the directions shown, producing a strain flow at the bubble in the centre of the mill.

that of the exterior fluid, so that the drop could be treated as an essentially inviscid bubble. Although the bubble was ellipsoidal in shape at low rotation rates, there existed a critical rotation rate $Q = 0.41$ at which the bubble suddenly developed pointed ends. Taylor noted that in fact this state was not a true steady state as 'a thin skin appeared to slip off the bubble surface'. Later experiments (see e.g. de Bruijn 1993 and references therein) showed that jets or small bubbles may be emitted from the pointed ends, a process known as tip streaming. After a certain time had passed (holding the rotation rate constant) Taylor observed that the rounded bubble ends re-emerged, and the resulting steady bubble was smaller than the original one. This rounded configuration persisted until $Q = 0.65$, at which point the ends once again suddenly became pointed. This new pointed configuration remained stable; at the maximum attainable strain ($Q = 2.45$) the drop still showed no sign of tip streaming or burst. The experiment was repeated and extended by others with similar results (see e.g. Torza, Cox & Mason 1972; Grace 1982; de Bruijn 1993), although in some cases the tip streaming is absent (Bentley & Leal 1986).

Analytical solutions for a three-dimensional bubble in slow viscous flow are not at present known, although asymptotic analysis using a slender drop assumption in axisymmetric flow has been performed by several authors (see e.g. Buckmaster 1972; Acrivos & Lo 1978; Hinch & Acrivos 1979; Sherwood 1984). However, these analyses encounter difficulties in resolving details of the flow and drop shape near the pointed ends. As a result, theoretical and computational studies of singularity formation in Stokes flow have mostly been limited to steady flow in two dimensions. Singularity formation on a free surface produced by counter-rotating cylinders in various classes of steady flows has been considered in Joseph *et al.* (1991), Joseph (1992), Jeong & Moffatt (1992), and Antanovskii (1996). In many cases explicit steady solutions have been provided by employing complex-variable techniques. Most relevant to the present study is the work by Antanovskii (1996), which includes a remarkable class of explicit steady solutions to a two-dimensional model of evolution in a four-roller mill which takes into account the rotational nature of the far–field flow. The steady bubbles are parameterized by the capillary number Q and a second non-dimensional parameter $\epsilon = CR^2/L^2$, where R is the undeformed bubble radius, L is the half-size of the mill side, and C is a dimensionless constant. For finite capillary number Q and all $\epsilon > 0$ the steady bubble interface is found to be smooth but for Q large enough possesses regions of high curvature that exhibit the form of apparent cusps; these

are expected to become true cusps in the limit of vanishing surface tension. Similar behaviour is obtained in the other cited examples of flow due to counter-rotating cylinders. Related analyses of two-dimensional flows include Richardson (1968, 1973) and Buckmaster & Flaherty (1973).

Much less effort has been devoted to investigating the transient development of cusped interfaces. The evolution of contracting bubbles is considered in Tanveer & Vasconcelos (1995), and true cusp development is observed for zero surface tension, but is inhibited for positive surface tension. The unsteady version of some rotating cylinder flows is investigated via boundary integral numerical simulation by Pozrikidis (1997, 1998). Particular attention is paid to the unsteady evolution for zero surface tension (i.e. $Q \to \infty$) where the presumed existence of steady bubble solutions with true cusps suggests the possibility of spontaneous cusp formation during the transient evolution. However, employing Antanovskii's model of Taylor's four-roller mill, Pozrikidis observed neither steady nor unsteady cusped shapes during the transient deformation for vanishing surface tension. Instead, 'jets' were viewed to emerge from the bubble ends in a manner reminiscent of tip streaming. It was suggested that the steady shapes are stable only when Q is less than a critical value that depends on the particular details of the far-field flow. Due to numerical difficulties associated with the large interfacial curvature at the bubble tips, the value of this critical capillary number was not ascertained. Pozrikidis (1998) also considered the effect of variable surface tension, induced by the presence of surfactant, on the transient deformation of nearly cusped bubbles. Although the computations again were quite delicate owing to the large curvature, it was concluded that the presence of surfactant may cause the bubble tips to become pointed. It is important to note that whereas steady cusps may occur only for vanishing tension, transient cusps are allowed in principle for any value of tension. However, to our knowledge the only example of a true singularity in time-dependent flow for non-vanishing tension is that due to Richardson (1997), involving the coalescence of five liquid cylinders. Other analyses of time-dependent free surfaces in Stokes flow include Hopper (1990), Richardson (1992), and Howison & Richardson (1995).

In this paper, we address by combined analytical and numerical techniques the possible formation of singularities during the transient evolution of a two-dimensional bubble in Taylor's four-roller mill. First, the evolution of a clean bubble in Antanovskii's model of Taylor's four-roller mill is revisited. The question of the stability of the steady solutions is examined numerically. For the value of ϵ corresponding to the large initial bubble in Taylor's experiment, the steady-state solutions are found to be linearly stable for all values of Q. Furthermore, boundary integral simulations employing a quite general conformal map representation of the interface show that a circular initial bubble shape will evolve to the analytical steady solution for all values of Q. We also clarify the picture for $Q = \infty$. Here, the transient evolution starting from a circle is found to lead to an unsteady cusped bubble; indeed, it is shown that there is no physically acceptable steady shape for vanishing surface tension. The behaviour observed here therefore differs somewhat from the tip streaming instability observed for $Q = \infty$ in Pozrikidis (1997). The differences illustrate the truly delicate nature of computing the evolution of nearly cusped shapes. A possible reason for the disparities lies in an observed instability of the steady surface to finite-amplitude perturbations at large Q – this is further discussed in § 3.

Complex-variable methods are used to derive general properties of the time-dependent evolution both with and without surfactant in § 4. These results are in some sense a generalization of the theory developed for *linear* far-field flow in Siegel (1999) and Tanveer & Vasconcelos (1995), and potential flow in Antanovskii (1994*c*).

However, the application here to *nonlinear, rotational* far-field flow leads to an essential difference, which we now describe (the terms linear and nonlinear in this context are defined in § 2). In essence, all these theoretical results use a conformal map $z(\zeta, t)$ which maps the interior of a unit disk in the ζ-plane to the physical flow domain at the exterior of the bubble. The location of the free surface at a time t is given by $z(\zeta, t) = x(v, t) + \mathrm{i}y(v, t)$ for $\zeta = \mathrm{e}^{\mathrm{i}v}$ on the arc of the circle. In the case of linear or potential flow, two important results provide a framework for the transient theory. One is that there is no spontaneous generation of singularities of z in the complex plane, and secondly no singularities move into the finite complex plane from infinity. Unfortunately, neither of these results holds for the far-field flow considered in this paper. However, we show that these properties do hold for a particular class of conformal maps, which form a dense set in the class of all smooth initial shapes. The importance of this lies in the fact that, within this class, the infinite-dimensional dynamical system for the evolving interface reduces to an 'exact solution' composed of a finite-dimensional system of ODEs for the motion of singularities and the time evolution of their amplitudes.

We also investigate whether variable surface tension, as induced by the presence of surfactant, may promote true singularity formation during time-dependent evolution. The motivation for this study comes from the experiments of de Bruijn (1993), which suggest that unsteady cusp formation followed by tip streaming only occurs when interfacial tension gradients develop, for example due to the presence of surfactant. The investigations here may be viewed as a continuation of the author's earlier paper (Siegel 1999), in which exact solutions for the *steady* deformation of a two-dimensional bubble with surfactant are derived. In contrast to the clean flow problem, the steady solution branches were found to terminate, with the termination point corresponding to a bubble with a true cusp (i.e. infinite curvature). This behaviour implies that there is an upper bound Q_c on the strain rate for which a steady bubble solution can exist. It was suggested that for larger strains, the time-dependent evolution would lead to unsteady cusp-shaped profiles, much like that seen in experiments. However, time-dependent solutions were not obtained. Previously, Antanovskii (1994*a*) considered the effect of surfactant on the steady interfacial profiles induced by a pair of counter-rotating point vortices below a free surface, although again the transient evolution was not considered.

In the present paper, the time-dependent evolution of the bubble and surfactant distribution is obtained using the reduced evolution equations derived in § 4. This enables general deductions to be made concerning the motion and allows the interfacial evolution to be computed nearly up to cusp formation. After a brief summary of the steady-state results in Siegel (1999) and their extension to include surface diffusion of surfactant, numerical simulations in § 5 of the transient evolution for $Q > Q_c$ show that the bubble reaches an unsteady cusped formation, much as in Taylor's experiments. Such a bubble can be viewed as a precursor to tip streaming. Our solutions show that the presence of positive but variable surface tension leads to time-dependent cusps in situations for which constant surface tension does not produce cusps. Comparison with experiment shows some intriguing similarities, despite the drastic simplifications employed in the model.

2. Governing equations

Consider an inviscid bubble placed in two-dimensional slow viscous flow. The bubble is considered to be neutrally buoyant, so that gravitational effects can be

ignored. The fluid outside the bubble has a large viscosity μ and is taken to be incompressible, whereas the fluid inside the bubble is assumed to have negligible viscosity. Thus the bubble pressure is constant; without loss of generality the constant is chosen to be zero. Neglecting inertial effects, the fluid motion is governed by the Stokes equations

$$\mu\nabla^2\boldsymbol{u} = \nabla p, \quad \nabla\cdot\boldsymbol{u} = 0, \tag{1}$$

where $\boldsymbol{u}(x, y)$ is the fluid velocity and p is the pressure.

On the bubble boundary the kinematic condition $\boldsymbol{u}\cdot\boldsymbol{n} = U_n$ holds, where U_n is the normal velocity of the interface. In addition we require a balance of stresses, which is written as

$$-p\boldsymbol{n} + 2\mu\boldsymbol{n}\cdot\boldsymbol{S} = \sigma\kappa\boldsymbol{n} - \nabla_s\sigma, \tag{2}$$

where $\boldsymbol{n}$ is the outward normal unit vector, $\boldsymbol{S}$ is the rate-of-strain tensor whose j,k component is given by $s_{j,k} = (1/2)(\partial u_j/\partial x_k + \partial u_k/\partial x_j)$, κ is the interfacial curvature, σ is the surface tension, and ∇_s is the surface gradient operator. The last term in (2) represents the Marangoni stress resulting from a non-uniform surface tension.

The bubble is considered to contain a fixed amount of insoluble surfactant. The relationship between the surface tension and surfactant concentration (measured in units of mass of surfactant per unit of interfacial length) is given by an equation of state of the form $\sigma = \sigma(\Gamma)$. Typically a linear equation of state is employed to examine the effect of surfactant on bubbles in extensional flows. Such a relationship is valid for dilute surfactant concentrations. However, for large non-dimensional strain Q the surfactant accumulates near convergent stagnation points in the flow and so the surfactant concentration can no longer be considered dilute. For this reason a nonlinear equation of state is more appropriate. Although there is a large number of nonlinear equations available in the literature, any of these may be incorporated into the general theory developed here. For definiteness we choose to employ the Langmuir equation (Edwards, Brenner & Wasan 1991)

$$\sigma = \sigma_0[1 + \beta\ln(1 - \Gamma/\Gamma_\infty)],$$

where σ_0 is the surface tension of the clean interface, Γ_∞ is the maximum concentration of surfactant (producing complete coverage of the bubble as a unimolecular film), and β is a dimensionless parameter defined by $\beta = RT\Gamma_\infty/\sigma_0$, with R the gas constant and T the temperature. Strictly speaking, this equation applies for soluble surfactant. However, it has been previously used in studies involving insoluble surfactant (Milliken, Stone & Leal 1993).

An equation describing the time-dependent behaviour of Γ is also required. It takes the form of a convection–diffusion equation (see Wong, Rumschitzki & Maldarelli 1996)

$$\left.\frac{\partial\Gamma}{\partial t}\right|_s - \frac{\partial\boldsymbol{X}}{\partial t}\cdot\nabla_s\Gamma + \nabla_s\cdot(\Gamma\boldsymbol{u}_s) - D_s\nabla_s^2\Gamma + \Gamma\kappa\boldsymbol{u}\cdot\boldsymbol{n} = 0, \tag{3}$$

where ∇_s is the surface gradient, $\boldsymbol{u}_s$ represents the velocity vector tangent to the interface, $\boldsymbol{X}(s,t)$ is a parametric representation of the interface, and D_s is the surface diffusivity. Here we have considered the surfactant to be insoluble, i.e. there is no net flux of surfactant to and from the interface from the bulk liquid.

To complete the problem statement, the following flow is specified at infinity:

$$\left.\begin{aligned}\boldsymbol{u}_\infty &= (Gx + G_1[x^3 + 3xy^2], -Gy - G_1[3x^2y + y^3]),\\ p_\infty &= P_\infty + 6G_1\mu(x^2 - y^2),\end{aligned}\right\} \tag{4}$$

where G and G_1 are parameters characterizing the rate of strain and P_∞ is an as yet undetermined pressure at the mill centre. This form of the far-field flow was determined by Antanovskii (1996), who used a boundary integral method to numerically compute the two-dimensional velocity field produced by the four rotating rollers when no drop is present. This was then used to obtain the parameters in a local expansion of the flow field at the centre of the mill. The result is expression (4), which is used as the far field for the inner flow around a drop in an unbounded fluid. Note that this far-field flow is the superposition of a linear (pure strain) velocity field, characterized by rate of strain parameter G, and a *rotational* motion described by cubic terms, characterized by the additional rate-of-strain parameter G_1.

The preceding problem can be recast in terms of non-dimensional quantities if the velocity is rescaled by GR (where πR^2 is the initial bubble area), surface tension by σ_0, pressure by $G\mu$, surfactant concentration by Γ_∞, and length and time by R and $1/G$. The problem is then completely characterized by the dimensionless parameters

$$Q = \frac{2\mu GR}{\sigma_0}, \quad \epsilon = \frac{G_1 R^2}{G} = \frac{CR^2}{L^2}, \quad Pe_s = \frac{\sigma_0 R}{\mu D_s}, \quad \chi = \frac{\Gamma_i}{\Gamma_\infty}, \text{ and } \beta,$$

where Q is the non-dimensional strain (Q is of the form of a capillary number), Pe_s is the modified surface Péclet number and $2\pi\Gamma_i$ is the fixed amount of surfactant on the bubble surface.†

2.1. *Complex-variable formulation*

The complex-variable representation of two-dimensional Stokes flow has been widely employed to study the motion of drops and bubbles in various flows (see e.g. Hopper 1991; Richardson 1992; Tanveer & Vasconcelos 1995 and references therein). As the formulation of Siegel (1999) is easily modified to account for the cubic terms in the far-field flow, we present the relevant formulas here without derivation.

Introduce the stress–stream function $W(z,\bar{z}) = \phi(x,y) + \mathrm{i}\psi(x,y)$ where $z = x + \mathrm{i}y$ and the bar denotes complex conjugate. It is well known that for Stokes flow ϕ and ψ satisfy the biharmonic equation. According to the Goursat representation for biharmonic functions (Mikhlin 1957) $W(z,\bar{z})$ can be written $W(z,\bar{z}) = \bar{z}f(z) + g(z)$ where f and g are analytic functions in the fluid region. We observe that the form of the far-field flow (4) computed by Antanovskii (1996) leads to the following non-dimensional expression for the stress–stream function as $z \to \infty$:

$$W_\infty(z) = \frac{1}{2}\left[(1 + \epsilon|z|^2)z^2 + \frac{p_\infty}{2}|z|^2\right]. \tag{5}$$

The far-field flow is called *nonlinear* if $f(z)$ or $g'(z)$ behave at infinity like a nonlinear polynomial in z, which is the case in (5). In general the far-field flow has a rotational component when f is nonlinear in z.

At this point it is convenient to consider a conformal map $z(\zeta,t)$ which takes the unit disc in the ζ-plane into the fluid region of the z-plane. This map can be written in the form

$$z(\zeta,t) = \frac{\gamma_0(t)}{\zeta} + h(\zeta,t), \tag{6}$$

† Alternatively, the velocity may be rescaled by σ_0/μ, pressure by σ_0/R, and time by $R\mu/\sigma_0$. The modified Péclet number is related to the usual Péclet number $Pe = GR^2/D_s$ by $Pe = QPe_s/2$. The modified Péclet number is preferable in studies of shear-induced drop deformation, since it depends on material properties only.

where h is analytic and $z_\zeta \neq 0$ in the region $|\zeta| \leqslant 1$ over some non-zero time interval. The extra degree of freedom allowed by the Riemann Mapping Theorem permits γ_0 to be chosen real and positive. Symmetry about the x- and y-axes is enforced by requiring

$$-z(-\zeta) = z(\zeta), \quad \bar{z}(\bar{\zeta}) = z(\zeta). \tag{7}$$

Note that the form (6) of the map z and the far-field condition (5) imply that

$$f(\zeta,t) \sim \frac{\epsilon\gamma_0^3}{2\zeta^3} + \frac{p_\infty\gamma_0}{4\zeta} + O(1), \quad g'(\zeta,t) \sim \frac{\gamma_0}{\zeta} + O(1) \tag{8}$$

as $\zeta \to 0$.

After writing the physical quantities in terms of f and g as in Tanveer & Vasconcelos (1995) and Siegel (1999), the kinematic boundary condition can be shown to have the form

$$\mathrm{Re}\left\{\frac{z_t + 2f}{\zeta z_\zeta} + \frac{\epsilon\gamma_0^2}{\zeta^2}\right\} = \frac{\tau}{Q|z_\zeta|} + \mathrm{Re}\left[\frac{\epsilon\gamma_0^2}{\zeta^2}\right] \tag{9}$$

on $|\zeta| = 1$, where $\tau = 1 + \beta\ln(1-\Gamma)$ is the non-dimensional surface tension. Note that the term $\mathrm{Re}\,[\epsilon\gamma_0^2/\zeta^2]$ has been added to both sides of the kinematic equation to remove the singularity from the term in braces. This singularity is a consequence of the cubic nature of the far-field flow; no additions are necessary for linear flow, and other additions can be made to remove the singularity for higher-order flows. An evolution equation for the map $z(\zeta,t)$ in $|\zeta| < 1$, which is useful in the general theory developed in § 4, can now be obtained by an application of the Poisson Integral Formula (Mikhlin 1957) to (9), with the result

$$z_t + 2f(\zeta,t) = \zeta z_\zeta\left[\frac{-\epsilon\gamma_0^2}{\zeta^2} + I(\zeta,t)\right], \tag{10}$$

where

$$I(\zeta,t) = \frac{1}{2\pi\mathrm{i}}\oint_{|\zeta'|=1}\frac{\mathrm{d}\zeta'}{\zeta'}\left[\frac{\zeta'+\zeta}{\zeta'-\zeta}\right]\left\{\frac{\tau(\zeta',t)}{Q|z_\zeta(\zeta',t)|} + \mathrm{Re}\left[\frac{\epsilon\gamma_0^2}{\zeta^2}\right]\right\}. \tag{11}$$

Note that $I(\zeta,t)$ depends on the surfactant distribution via the term $\tau(\zeta',t)$ in the integrand.

Equation (10) describes the time evolution of the conformal map in a way that is useful in the general theory. However, for the purposes of computing the map $z(\zeta,t)$ a different form of the evolution equation is more convenient. This is derived from the dynamic boundary condition following Tanveer & Vasconcelos (1995) with the result

$$g'(\zeta,t) = \frac{\bar{z}(\zeta^{-1},t)}{2}\left\{\frac{z_{\zeta t}(\zeta,t)}{z_\zeta(\zeta,t)} - \zeta\left[I_\zeta(\zeta,t) + \frac{2\epsilon\gamma_0^2}{\zeta^3}\right] - \left[1 + \frac{\zeta z_{\zeta\zeta}(\zeta,t)}{z_\zeta(\zeta,t)}\right]\left[I(\zeta,t) - \frac{\epsilon\gamma_0^2}{\zeta^2}\right]\right\}$$
$$+\frac{1}{2}\left\{\frac{\bar{z}_\zeta(\zeta^{-1},t)}{\zeta}I(\zeta,t) + \bar{z}_t(\zeta^{-1},t) + \bar{z}_\zeta(\zeta^{-1},t)\frac{\epsilon\gamma_0^2}{\zeta^3}\right\}, \tag{12}$$

which is originally valid on the unit circle but is extended off through analytic continuation. Note that in the case of linear far-field flow, with $\epsilon = 0$, the expression (12) agrees with that previously derived in Tanveer & Vasconcelos (1995). The requirement that the right-hand side of (12) is analytic in $|\zeta| < 1$ (except for a known singularity at $\zeta = 0$) determines the time evolution of the map $z(\zeta,t)$. Explicit evolution equations for the map parameters such as $\gamma_0(t)$ in some special cases will be provided in § 4.

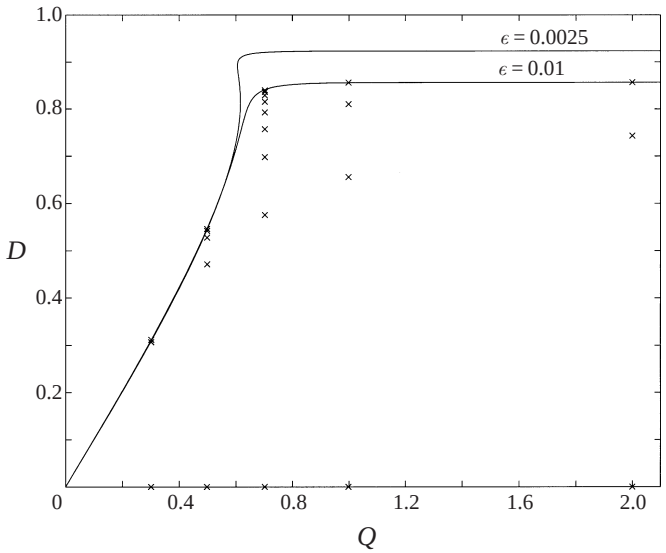

FIGURE 2. The dependence of deformation D on capillary number Q for Antanovskii's steady-state solution (i.e. no surfactant). Branches are shown for $\epsilon = 0.01$ and $\epsilon = 0.0025$. Also shown is the transient evolution for $\epsilon = 0.01$, computed using the general conformal map method. For each Q, the crosses represent the deformation of a time-evolving bubble starting from a circle ($D = 0$) at $t = 0$. The time increment between crosses is $\Delta t_m = 0.75$. The transient solution converges to the steady state for all finite Q.

Finally, the complex-variable formulation of the equation for $\Gamma(\zeta = \mathrm{e}^{\mathrm{i}v}, t)$ is obtained from the non-dimensional version of (3). The result is

$$\left.\frac{\partial \Gamma}{\partial t}\right|_v - \mathrm{Re}\left(\frac{\Gamma_v}{z_v} z_t\right) + \frac{1}{|z_v|}\frac{\partial}{\partial v}\mathrm{Re}\, P(v,t) - \frac{1}{|z_v|}\mathrm{Im}\left(\frac{z_{vv}}{z_v}\right)\mathrm{Im}\, P(v,t) = \frac{2}{QPe_s}\frac{1}{|z_v|}\frac{\partial}{\partial v}\left(\frac{\Gamma_v}{|z_v|}\right), \quad (13)$$

where $P(v,t) = (u_1 + \mathrm{i}u_2)\bar{z}_v \Gamma / |z_v|$ and $u_1 + \mathrm{i}u_2$ is the complex velocity. The function Γ is required to satisfy the imposed symmetries $\Gamma(-v,t) = \Gamma(v,t)$ and $\Gamma(\pi + v, t) = \Gamma(v,t)$. Note that the total amount of surfactant is fixed, so that the integral

$$T = \int_0^{2\pi} \Gamma |z_v| \mathrm{d}v \quad (14)$$

is a conserved quantity.

3. Transient evolution, clean flow problem

In this section we consider the transient evolution of an arbitrary bubble shape immersed in the far-field flow (5), when surfactant is absent. Previously, Pozrikidis (1997, 1998) considered the process of cusp formation in this flow using an adaptive boundary integral method which explicitly incorporated the four-fold bubble symmetry. We briefly summarize his results in the case $\epsilon = 0.01$, which corresponds to the value of ϵ for the larger initial bubble in Taylor's experiment (Antanovskii 1996).

Define the deformation of the bubble by

$$D = \frac{R_{max} - R_{min}}{R_{max} + R_{min}},$$

where R_{max} and R_{min} are the maximum and minimum distances from the origin to a point on the bubble surface. The steady solution branch determined by Antanovskii for $\epsilon = 0.01$, represented by plotting D versus Q, is shown is figure 2. The leftmost portion of the curve, between $Q = 0$ and $Q = 0.6$, represents rounded bubble profiles. In contrast the bubble shapes along the flat upper portion of the curve are cusp-like (although smooth) and show a remarkable similarity with the bubble profiles observed in the experiments of Taylor. When Q is less than 0.6, Pozrikidis observed the bubble to evolve into the steady-state solution, with excellent agreement between the theoretical and numerical steady profile. At finite Q greater than about 0.7, numerical difficulties associated with the large curvature at the bubble tips prevented the computation from continuing for long enough times to reach the steady state. More interesting phenomena are noticed for vanishing surface tension ($Q = \infty$), at which the bubble is observed to evolve toward a cusped configuration but before the curvature gets too large the bubble develops two symmetric necks and ejects 'jets' into the fluid in a process reminiscent of tip streaming. The $Q = \infty$ evolution never resulted in a truly cusped profile, steady or unsteady. This behaviour led Pozrikidis to conjecture that the theoretical steady shapes are stable only when Q is less than a critical capillary number, the value of which depends on ϵ. Numerical difficulties stemming from the large interfacial curvature prevented a determination of the critical value.

We investigate this conjecture by performing two tasks. First, the linear stability of the theoretical steady solutions is examined. Define the perturbation $\tilde{z}$ by

$$z(\zeta, t) = z^s + \eta\tilde{z} \tag{15}$$

where z^s denotes a particular steady solution and $|\eta| \ll 1$. This function $\tilde{z}$ is expanded in a Laurent series as

$$\tilde{z} = \sum_{j=-1}^{\infty} a_j(t)\zeta^j. \tag{16}$$

In the standard way, the evolution equations for $\tilde{z}$ linearized about z_s admit normal mode solutions of the form $a_j(t) = e^{\sigma t}\hat{a}_j$. As discussed in Appendix A, an appropriate discretization of the linearized evolution equations leads to a generalized eigenvalue problem for the eigenvalue σ and truncated eigenvector $(\hat{a}_{-1}, \ldots, \hat{a}_{N-2})^T$, which is easily solved. Note that if the symmetry restrictions (7) are applied to the perturbation $\tilde{z}$, then $\hat{a}_j$ is real and satisfies $\hat{a}_j = 0$ for j an even integer.

The numerical method is verified by checking that in the limit $Q \to 0$ the results agree with analytically computed eigenvalues $\sigma_k = -k/Q$ for $k = 0, \ldots, N-1$ with corresponding eigenvectors $\hat{a}_j = 1$ if $j = k - 1$ and $\hat{a}_j = 0$ otherwise. A comparison of the numerical results for $N = 1024$ and $N = 512$ shows that the 16 smallest eigenvalues (in absolute value) and their corresponding eigenvectors are accurate to nine digits. The results of the linear stability calculation for four-fold symmetric bubbles at $\epsilon = 0.01$, corresponding to the calculations of Pozrikidis (1998), are shown in figure 3. This figure depicts the three largest non-zero eigenvalues for a range of Q. The key feature is that σ_k is negative for all k, indicating stability for linear theory. No linearly unstable modes were found for finite Q in the symmetric case. It is interesting to note that if the reflection symmetry about the y-axis is relaxed, so that the perturbation $\tilde{z}$ is allowed to contain even powers of ζ, then the evolution

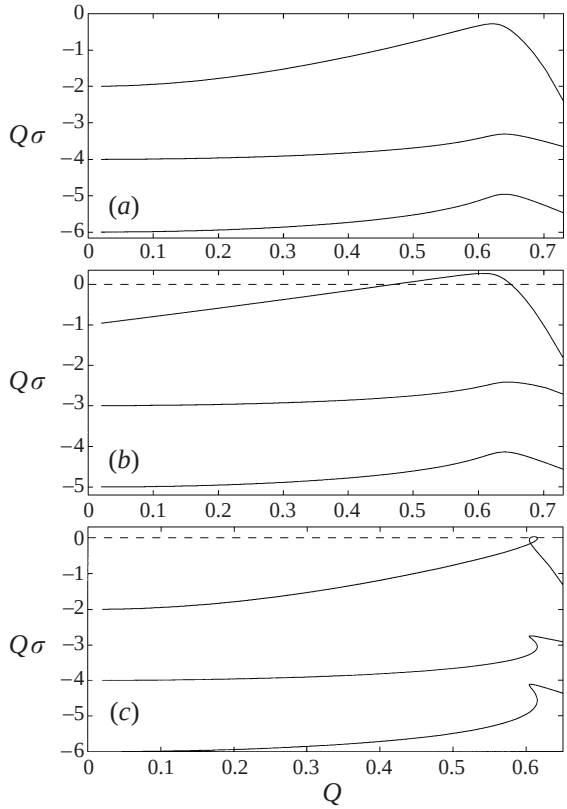

FIGURE 3. The three largest non-zero eigenvalues to the linearized evolution equations, plotted versus Q. (*a*) Four-fold symmetric bubbles with $\epsilon = 0.01$. (*b*) Asymmetric bubbles, with the reflection symmetry about the y-axis relaxed ($\epsilon = 0.01$). (*c*) Four-fold symmetric bubbles with $\epsilon = 0.0025$.

becomes linearly unstable for a range of Q. Figure 3(*b*) depicts the largest eigenvalues for an asymmetric perturbation $\tilde{z}$ containing only even powers of ζ. The dominant component of the unstable eigenvector corresponds to a pure translational motion of the bubble. This instability is in fact observed in experiments, but is easily controlled by slightly varying the relative speed of the rollers (Taylor 1934).

At smaller ϵ (i.e. $\epsilon < 0.004$) the $D(Q)$ curve is no longer monotonic. For example, figure 2 shows the steady-state response curve for $\epsilon = 0.0025$, corresponding to the second, smaller, steady bubble in Taylor's experiment (Antanovskii 1996). Antanovskii hypothesized that the upper and lower solution branches are stable. This implies a hysteresis loop where there is a transition from a steady rounded bubble on the lower branch to a steady cusp-like one on the upper branch at the turning point $Q = Q_t$, with the reverse transition occurring at the upper-branch turning point. However, simulations in Pozrikidis (1998) suggest that the lower branch is stable while the upper branch for $Q > Q_t$ is unstable, consistent with the conjecture of a critical capillary number for instability. The results of our linear stability calculation for a four-fold symmetric bubble with $\epsilon = 0.0025$ are shown in figure 3(*c*). There is a band of positive eigenvalues for $0.605 < Q < 0.615$ associated with the portion of the response curve between the turning points, indicating that this branch is unstable. However, we find that the upper branch is linearly stable at least up to $Q = 0.7$, which was the maximum Q considered when $N = 1024$. Transient simulations described subsequently

show that the upper branch is in fact stable to small perturbations for all finite Q. This supports the physical relevance of the hysteresis loop. The instability of the upper branch observed in Pozrikidis (1998) illustrates a sensitivity to perturbations for nearly cusped interfaces, which becomes more pronounced as the steady interface approaches a true cusp. This is further elaborated later in this section.

Nonlinear stability is investigated by computing the transient evolution starting from an arbitrary smooth initial shape. We employ a boundary integral method, described in Appendix A, that is basically similar to that described in Antanovskii (1994*b*) but with a few improvements that let us effectively compute bubbles even with very sharp ends. The method utilizes the conformal map parameterization, but is quite general in that no assumptions are made concerning the form of the map. We note that it is critical to apply a dealiasing procedure that is described there. Without this procedure inaccuracies can develop over time and lead to termination of the code. The number of points N in the discretization of z can be kept quite small, since the cusp corresponds to a zero of z_ζ and singularities in $z(\zeta, t)$ are far from the unit disk. In this sense the conformal map parameterization is optimal. The numerical method is checked by comparing the computed solution, starting from an initially circular bubble, with that obtained from a more specialized code that utilizes the reduced representation discussed in § 4. The two methods are found to be in complete agreement.

Figure 2 also depicts the time-dependent deformation of a circular bubble, for $\epsilon = 0.01$ and various Q values. At a given Q, the crosses represent the bubble deformation at discrete times separated by an interval of 0.75. The uppermost cross for each Q represents the computed steady deformation, i.e. the cross position for still larger t does not change enough to be observable on the plot. Clearly there is excellent agreement between the theoretical and numerically computed steady deformation. We take this agreement as additional verification of the numerical method for general z. Although for purposes of illustration figure 2 is restricted to the range $0 \leqslant Q \leqslant 2$, our numerical simulations show that an initially circular bubble is attracted to the theoretical steady-state solution for all finite values of Q.

The bubble deformation in the case $Q = \infty$ is shown in figure 4. The bubble evolves toward a cusped configuration (figure 4*a*) with rapid growth in the curvature (figure 4*b*). The general theory of § 4 shows that a physically acceptable steady solution does not exist here, and the considerations of that section combined with the simulations here lead us to conclude that for $Q = \infty$ the dynamics results in unsteady cusp formation. Near the critical time t_c for blow up, the functional form of the curvature is given by $\kappa \sim c(t_c - t)^{-2}$, where t_c is estimated to be 0.935 (see inset, figure 4*b*). Unlike the calculations of Pozrikidis (1997, 1998), we do not observe a tip streaming instability when starting from an initially circular bubble. The differences in behaviour may be due to the differing parameterizations employed in the respective calculations. The conformal map parameterization used here provides a particularly compact representation of the interface, i.e. it requires only a few Fourier modes to accurately represent the cusp singularity. A different parameterization, such as one using an arclength variable, will require many modes to accurately represent a cusping interface. The evolution may then be sensitive to small errors in the large-k modes. Such errors, which are present due to roundoff, truncation and time-differencing errors may smooth the cusp and allow the evolution to continue beyond the singularity. In addition, point insertion at regions of large curvature may be a smoothing operation. Ceniceros & Hou (2000) discuss similar issues and advantages of conformal map parameterization in the Hele-Shaw problem.

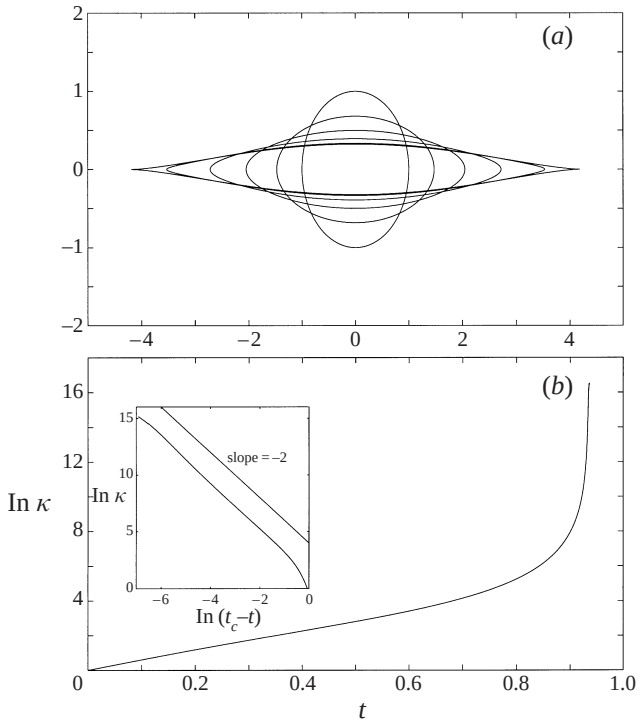

FIGURE 4. (*a*) Bubble evolution for $Q = \infty$. The time increment between profiles is $\Delta t_m = 0.2$, with the final increment $\Delta t_m = 0.134$. (*b*) Plot of the curvature at the bubble ends for the evolution in (*a*). Inset: the approach to the singularity is described by the functional form $\kappa \sim c(t_c - t)^{-2}$, where $t_c = 0.935$ is the estimated critical time.

Although we do not explore this conjecture further, an illustration of the sensitivity of the evolution to small finite-amplitude perturbations is given in figure 5. There the motion starting from a slightly perturbed circular bubble of the form $z(\zeta, 0) = 1/\zeta - 0.01/\zeta^9$, with $Q = \infty$ is depicted. Instead of reaching a steady state, the bubble generates narrow jets which eventually pinch off, indicating bubble breakup (see Tanveer & Vasconcelos 1995 for a discussion of bubble breakup in contracting bubbles). This behaviour is somewhat similar to that observed in Pozrikidis (1997, 1998) for circular-bubble initial data, although the jets here are much finer. Nevertheless, this behaviour is suggestive of the role that perturbations in the higher modes can have on the resulting bubble evolution.

In general, it is observed that a rather large class of perturbations from a steady bubble configuration results in dynamics leading to interfacial pinch-off or the formation of true cusp singularities (to numerical resolution), rather than returning to the steady state. This is the case, provided the perturbation is not too small and the capillary number is sufficiently large. Thus, the steady bubble solutions, though linearly stable, are subject to finite-amplitude instability for a wide class of perturbations and Q sufficiently large. (On the other hand, perturbations to the steady state – even quite large ones – along certain directions in phase space would ultimately evolve back to the appropriate steady solution; the attraction of an initially circular bubble to the steady-state solution is one example.) Note that there are none of the nearby (linearly) unstable steady states that usually accompany finite-amplitude

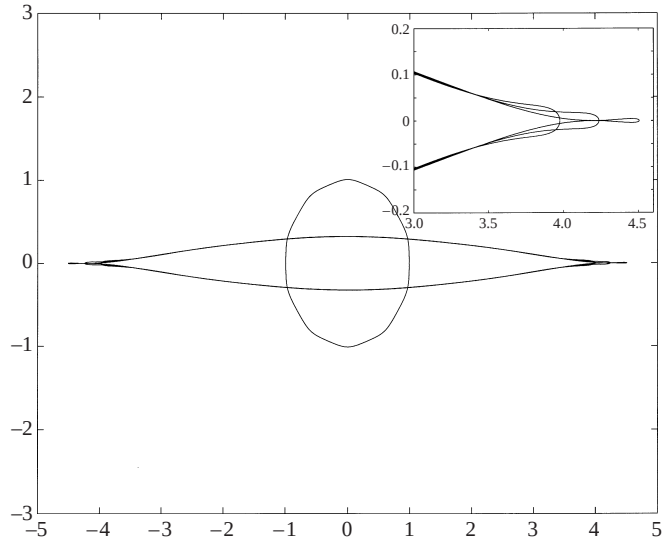

FIGURE 5. Evolution of a perturbed circular bubble at $Q = \infty$. Initial data are of the form $z(\zeta, 0) = 1/\zeta - 0.01/\zeta^9$. Profiles are shown for $t = 0.9$, 0.95, 0.9975. (Inset shows details of the pinch-off.)

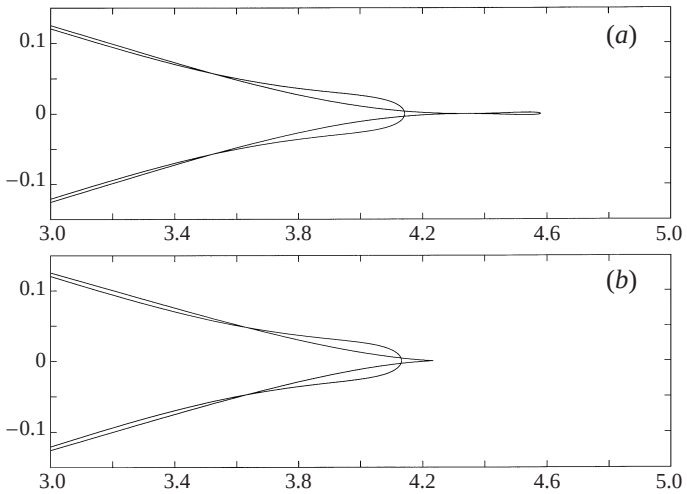

FIGURE 6. Evolution of a multi-mode perturbation to the steady, nearly cusped bubble for different values of the capillary number Q. (*a*) $Q = 80$: the evolution leads to tip streaming. (*b*) $Q = 1.2$: the perturbed bubble relaxes to the steady near cusp shape.

instability. There are some indications that the amplitude of a given perturbation exciting instability decreases as Q increases. For example, figure 6 shows the progress of a multimode perturbation for two different values of Q. At the larger value of Q, the perturbation leads to tip streaming. However, as Q is reduced, the tip streaming is suppressed and the bubble returns to the steady state. It does not appear that the amplitude of a perturbation leading to instability tends to zero as $Q \to \infty$, although this awaits further analysis.

4. General properties of time-dependent evolution and exact solutions

Analytic continuation of (10) into the domain $|\zeta| > 1$ is useful for deriving global properties of the mapping function $z(\zeta, t)$ and general features of the time-dependent evolution. The continuation is implemented in the usual way using contour deformation, and leads to the equation (see Tanveer & Vasconcelos 1995; Siegel 1999 for related results)

$$z_t = q_1 z_\zeta + q_2 + q_3 z, \tag{17}$$

where the functions $q_1(\zeta, t)$ to $q_3(\zeta, t)$ and their asymptotic behaviour as $\zeta \to \infty$ (which is useful in the subsequent discussion) are given by

$$\left.\begin{aligned} q_1(\zeta, t) &= \zeta[I(\zeta, t) + \epsilon\gamma_0^2\zeta^2] \sim \epsilon\gamma_0^2\zeta^3 + O(\zeta), \\ q_2(\zeta, t) &= 2\bar{g}'(\zeta^{-1}, t) \sim 2\gamma_0\zeta + O(1), \\ q_3(\zeta, t) &= \frac{2\bar{f}_\zeta(\zeta^{-1}, t)}{\bar{z}_\zeta(\zeta^{-1}, t)} \sim 3\epsilon\gamma_0^2\zeta^2 + O(1). \end{aligned}\right\} \tag{18}$$

Equation (17) may be viewed as a hyperbolic equation for z in the complex region $|\zeta| > 1$, with characteristic curves defined by the function q_1. There is a key difference between the dynamics exhibited by (17), (18) and that for a bubble evolving in a linear far-field flow (Tanveer & Vasconcelos 1995; Siegel 1999), or for a bubble evolving in a nonlinear but irrotational far-field flow (i.e. with $g(z)$ a polynomial in z), considered in Antanovskii (1994*c*). For linear or irrotational flow, it is easily seen from the form of f and the analyticity of $I(\zeta, t)$ in the exterior of the unit disk that the functions $\zeta^{-1}q_1$ and q_3 are analytic in $|\zeta| > 1$ (including at infinity), and hence contain only non-positive powers of ζ in their Laurent series, while q_2 is analytic in the finite complex plane. A number of important consequences follow. Among the most important for the general theory are that the form of pole and branch point singularities of z in the finite complex plane are invariant with time, and that these singularities move away from the unit disk; in particular no singularities move into the finite complex plane from infinity. These properties allow the construction of simple exact solutions for $\zeta z(\zeta, t)$ that are polynomials in ζ. The nonlinearity of $f(z)$ leads to the presence of terms of $O(\zeta)$ and larger in the expressions for $\zeta^{-1}q_1$ and q_3 and erases these conclusions, so that in general singularities will be generated at infinity and move toward the unit disk. To illustrate this latter fact, note that the evolution of a singularity located at ζ_j is determined from $\dot{\zeta}_j = -q_1(\zeta_j(t), t)$ (see equation (20)). For $|\zeta_j| \gg 1$ it follows from (11) that

$$q_1(\zeta_j, t) = -\zeta_j\left[\epsilon\gamma_0^2\zeta_j^2 - \frac{1}{Q\gamma_0}\right] + O(1).$$

Keeping only the leading-order term in ζ_j and integrating the differential equation for ζ_j then leads to

$$\zeta_j \sim \frac{1}{(2\epsilon\gamma_0^2 t + \zeta_j^{-2}(0))^{1/2}}$$

for small t. Thus, for small times a singularity generated at large $|\zeta|$ moves toward the unit disk, with the exception of any singularity for which $\mathrm{Re}\,\zeta_j^{-2}(0) < 0$.

Despite this behaviour, there nevertheless exists a very broad class of initial data for which the number and form of singularities in $|\zeta| > 1$ is preserved in time. The usefulness of this fact is evident: given a member of this class, the infinite-dimensional dynamical system for the function $z(\zeta, t)$ can be reduced into a finite-dimensional

dynamical system for the singularity locations and strengths. To describe this class, consider initial data of the form

$$z(\zeta,0)=\frac{E(\zeta,0)}{\zeta\prod_{j=1}^{N}\left(1-\dfrac{\zeta^2}{\zeta_j^2(0)}\right)} \tag{19}$$

where $E(\zeta,0)$ is analytic in the finite complex plane (although it may contain 'poles' at infinity) and the $\zeta_j(0)$ are complex numbers satisfying $|\zeta_j(0)|>1$. These quantities are subject to the restriction $z_\zeta\neq 0$ in the closed unit disk. The form (19) is the most general one describing a conformal map $z(\zeta,0)$, analytic in $|\zeta|\leqslant 1$ except for a pole singularity at $\zeta=0$, containing $2N$ pole singularities in $|\zeta|>1$, and satisfying the symmetries given in (7) (we use the convention $\zeta_{2j}=\overline{\zeta}_{2j-1}$ for $j=1,\ldots,N$ to satisfy the second requirement in (7)).

It is clear that for later times the evolution will be described by a map with the same form but with time-dependent quantities $E(\zeta,t)$ and $\zeta_j(t)$. The governing equations for these quantities are found by substitution into (17), with the result

$$E_t=q_1E_\zeta-q_1\frac{E}{\zeta}+2E\zeta\sum_{j=1}^{N}\left[\frac{\zeta_jq_1(\zeta,t)-\zeta q_1(\zeta_j,t)}{\zeta_j(\zeta_j^2-\zeta^2)}\right]+q_2\zeta\prod_{j=1}^{N}\left(1-\frac{\zeta^2}{\zeta_j^2}\right)+q_3E, \tag{20a}$$

$$\frac{\mathrm{d}\zeta_j}{\mathrm{d}t}=-q_1(\zeta_j,t). \tag{20b}$$

In general, initial data $E(\zeta,0)$ analytic in the finite complex plane will not remain so for later times. An exception occurs in the case when $E(\zeta,0)$ is a polynomial of order k, where $k\leqslant 2N$. To see this, suppose that

$$E(\zeta,t)=\sum_{j=0}^{N}\gamma_j\zeta^{2j} \tag{21}$$

for γ_j real and $N\geqslant 1$, which is the most general polynomial of order $2N$ exhibiting the desired symmetries. We show that this form for E is preserved over time. Introduce the projection operator P_N, which acts on functions $f(v)$ with a convergent Fourier series representation $f(v)=\sum_{n=-\infty}^{\infty}\hat{f}_n\mathrm{e}^{\mathrm{i}nv}$ and is defined by

$$P_Nf=\sum_{n=N+1}^{\infty}\hat{f}_n\mathrm{e}^{\mathrm{i}nv}.$$

The complex numbers $\hat{f}_n$ are the Fourier coefficients and v is in general complex (e.g. the region $|\zeta|>1$ corresponds to the lower half-plane of v). After applying the operator P_{2N} to (20*a*) and employing the asymptotic behaviour of q_i for $i=1,\ldots,3$, the projection $D=P_{2N}E$ is found to satisfy

$$D_t=2\gamma_0\zeta^{2N+2}(\epsilon\gamma_0\gamma_N+\delta_N),$$

where $\delta_N=\prod_{j=1}^{N}(-1/\zeta_j^2)$. It follows that if γ_N satisfies

$$\gamma_N=-\frac{\delta_N}{\gamma_0\epsilon}, \tag{22}$$

then D_t will be zero for all t. In this case, $E(\zeta,t)$ will remain a polynomial of degree at most $2N$ for all time, and only the $2N$ singularities at $\pm\zeta_j$ will be present in $|\zeta|>1$,

with time-dependent positions given by (20*b*). On the other hand if $E(\zeta,0)$ contains a term of $O(\zeta^{2N+m})$ for even integer $m \geqslant 2$, then the right-hand side of (20*a*) contains a non-zero term of $O(\zeta^{2N+m+2})$ and all higher (even) powers of ζ are generated in $E(\zeta,t)$. In this case the compact form of z is no longer preserved and new singularities may be generated. Note that the presence of surfactant influences equation (17) through the term $I(\zeta,t)$, but it does not alter any of the analytic properties and thus does not affect any of these conclusions.

It remains to be shown that (22) is in fact satisfied by the time-dependent evolution. This is most easily done by matching the form of the singularity in the governing equation (12) at $\zeta = 0$. To facilitate this task, we note the asymptotic behaviour of certain key terms in the limit $\zeta \to 0$ is given by

$$\left.\begin{aligned} &\bar{z}(\zeta^{-1},t) \sim \frac{\gamma_N}{\delta_N}\zeta + O(\zeta^3) \quad \bar{z}_t(\zeta^{-1},t) \sim \frac{\dot{\gamma_N}\delta_N - \dot{\delta_N}\gamma_N}{\delta_N^2}\zeta + O(\zeta^3) \\ &\bar{z}_\zeta(\zeta^{-1},t) \sim -\frac{\gamma_N}{\delta_N}\zeta^2 + O(\zeta^4). \end{aligned}\right\} \tag{23}$$

The asymptotic behaviour of $I(\zeta,t)$ at $\zeta = 0$ readily follows from the Taylor's expansion $I(\zeta,t) = I_0(t) + \sum_{k=1}^{\infty} \hat{I}_k(t)\zeta^k$, where (see (11))

$$I_0 = \frac{1}{2\pi Q}\int_0^{2\pi} \frac{\tau(v,t)}{|z_\zeta(\mathrm{e}^{\mathrm{i}v},t)|}\,\mathrm{d}v \quad \text{and} \quad \hat{I}_k = \frac{1}{\pi}\int_0^{2\pi}\left(\frac{\tau(v,t)}{Q|z_\zeta(\mathrm{e}^{\mathrm{i}v},t)|} + 2\epsilon\gamma_0^2\cos 2v\right)\mathrm{e}^{-\mathrm{i}kv}\,\mathrm{d}v. \tag{24}$$

Now, equating the coefficients of the $O(1/\zeta)$ terms in equation (12) yields, upon simplification, precisely the desired condition (22). Time-evolution equations for the remaining coefficients in (19), (21) are determined by enforcing the analyticity of the right-hand side of (12) in $0 < |\zeta| < 1$. Specifically, multiplying (12) by $[1-(\zeta\zeta_j)^{-2}]^p$ for $j = 1,\ldots,N$ and $p = 1,2$, then evaluating at $\zeta = \zeta_j^{-1}$, gives $2N$ relations among the $2N+1$ map parameters (with (22) supplying the final condition). It is easy to see that the $p = 1$ relations are simply (20). Unfortunately, the algebra is too complicated to obtain general formulae for the other coefficients in the case of $2N$ singularities exterior to the unit disk. However, we do present the formulae for the simplest case $N = 1$. This case includes the time evolution of circular initial data $z(\zeta,0) = \gamma_0(t)/\zeta$, for which two singularities are generated at infinity and at early times move toward the unit disk along the real axis.

For convenience denote the $N = 1$ conformal map by

$$z(\zeta,t) = \frac{\gamma_0 + \gamma_1\zeta^2}{\zeta(1-\gamma_2\zeta^2)}. \tag{25}$$

Evaluating condition (22) for $N = 1$ results in

$$\gamma_1 = \frac{\gamma_2}{\epsilon\gamma_0}. \tag{26}$$

The $p = 1$ relation is easily found to be

$$\dot{\gamma_2} = -2\gamma_2\left[I(\gamma_2^{1/2},t) - \frac{\epsilon\gamma_0^2}{\gamma_2}\right]. \tag{27}$$

An expression for $I(\gamma_2^{1/2},t)$ is derived in Appendix B; substituting this into (27) and

simplifying leads to

$$\dot{\gamma_2} = 2\gamma_2 \left[\epsilon\gamma_0^2 \left(\frac{1-\gamma_2^2}{\gamma_2} \right) - \frac{1-\gamma_2^2}{\pi Q} \int_0^\pi \frac{\tau(v',t)}{|\gamma_0(1-3\gamma_2 e^{iv'}) - \gamma_1 e^{iv'}(1+\gamma_2 e^{iv'})|} \, dv' \right] \tag{28}$$

which is the desired evolution equation for γ_2. Instead of performing the algebra necessary to obtain the $p = 2$ equation, we simply employ the condition that the drop area equal π (Antanovskii 1996). This leads to the third relation among the three map parameters

$$\gamma_0 = \left[\frac{2(1+\gamma_1^2)}{c_1 + (c_1^2 - c_2)^{1/2}} \right]^{1/2}, \tag{29}$$

where

$$c_1 = 1 - \epsilon\gamma_1^2[2(1-\epsilon) + \epsilon\gamma_1^2] \quad \text{and} \quad c_2 = 4\epsilon^2\gamma_1^2(1+\gamma_1^2)[3 + \epsilon(2+\epsilon)\gamma_1^2]. \tag{30}$$

In summary, the three equations (28), (26), and (29) determine the time evolution of the conformal map parameters $\gamma_i, i = 0, \ldots, 2$, in the $N = 1$ case. These parameters are functions of the surfactant concentration $\Gamma(\zeta, t)$, which in turn evolves according to equation (13). Note that the methods described in this section may be used to derive exact solutions for more general rotational far-field flows, such as when f is a general polynomial in z.

In contrast to the time-dependent evolution, the steady-state interfacial shape is necessarily restricted to the form of the $N = 1$ map (25), but with time-independent coefficients satisfying (26), (28) with $\dot{\gamma}_2 = 0$, and (29) (Antanovskii 1996). This result transcends the restriction to pole singularities implicit in the decomposition (19), and follows merely from the assumption of polynomial far-field flow of the form (5). Thus, to reach a steady state starting from initial data of the form (19), (21) with $N \geqslant 2$, all but two singularities must go off to infinity. An expression relating the capillary number Q to the steady interface shape and surfactant concentration is determined from equation (28) by setting $\dot{\gamma}_2 = 0$. This leads to

$$Q = \frac{\gamma_1}{\pi\gamma_0} \int_0^\pi \frac{\tau(v')dv'}{|\gamma_0(1-3\gamma_2 e^{iv'}) - \gamma_1 e^{iv'}(1+\gamma_2 e^{iv'})|}. \tag{31}$$

We also note that when $Q = \infty$ it is possible to evaluate the singularity velocity $q_1(\zeta_j, t)$ analytically. After doing so, the trajectory equation (20) becomes $\dot{\zeta}_j = \epsilon\gamma_0^2(\zeta_j^4 - 1)/\zeta_j$, which has equilibrium solutions at the four roots of unity. Clearly these steady solutions, corresponding to unclosed interfacial profiles, are unphysical. The form of the general time-dependent map suggests that the transient evolution for $Q = \infty$ will instead culminate in unsteady cusp formation or in a topological singularity, as is in fact observed in the simulations of § 3.

5. Bubble with surfactant

The effect of surfactant on the formation of cusped bubbles is now considered. A singular integral equation that determines the *steady* surfactant distribution was determined in Siegel (1999) and takes the form

$$\frac{i}{2}\mathscr{H}\left(\frac{\tau}{|z_v|}\right) = \frac{1}{Pe_s}\frac{\Gamma_v}{\Gamma|z_v|^2} + \epsilon Q\gamma_0^2 \sin 2v, \tag{32}$$

where $\mathscr{H}$ is the Hilbert transform, defined by $\mathscr{H}(f) = (1/2\pi i)\mathrm{PV}\int_0^{2\pi} f(v',t)\cot(v'-v)/2\,dv'$.

Depending on the non-dimensional strain and shape of the bubble, the surface can be either completely covered with surfactant or contain 'stagnant caps' of surfactant, i.e. regions where $\Gamma > 0$ interspersed with regions where $\Gamma = 0$ (Siegel 1999). Let $L = \{v : \Gamma(v) > 0\}$, and denote the complement of L by $\bar{L}$. From the imposed symmetry L consists of the intervals $[-\theta, \theta]$ and $[\pi - \theta, \pi + \theta]$, where θ needs to be determined as part of the solution. It is important to note that (32) holds only for $v \in L$.

5.1. *Steady bubbles: $Pe_s = \infty$*

An analytical solution for the steady bubble shape and surfactant distribution was determined in Siegel (1999) by applying a method based on the reduction of the singular integral equation to the so-called Riemann problem (Muskhelishvili 1953; Mikhlin 1957). In this section we present (without derivation) the exact solution and summarize its salient features, since these provide important clues to the expected outcome during transient evolution.

Given a steady interface shape, the exact solution to (32) takes the form

$$\frac{\tau}{|z_v|} = \frac{1}{|z_v|} + \tau_p + \mathrm{i}R_1(\alpha\omega - \bar{\alpha}/\omega). \tag{33}$$

The function τ_p is a particular solution to (32), given by

$$\tau_p(v) = \frac{\omega(v)}{2\pi\mathrm{i}}\,\mathrm{PV}\int_L \frac{r(v')}{\omega(v')}\cot\frac{(v'-v)}{2}\,\mathrm{d}v' + \frac{1}{2\pi\mathrm{i}\omega(v)}\mathrm{PV}\int_L r(v')\omega(v')\cot\frac{(v'-v)}{2}\,\mathrm{d}v', \tag{34}$$

where $\omega(\mathrm{e}^{\mathrm{i}v}) = [(\mathrm{e}^{\mathrm{i}v} - \bar{\alpha})(\mathrm{e}^{\mathrm{i}v} + \bar{\alpha})]^{1/2}\,[(\mathrm{e}^{\mathrm{i}v} - \alpha)(\mathrm{e}^{\mathrm{i}v} + \alpha)]^{-1/2}$ and $r(v) = (\mathrm{i}/2)\mathscr{H}(1/|z_v|) + \epsilon Q\gamma_0^2 \sin 2v$. Here $\alpha = \mathrm{e}^{\mathrm{i}\theta}$, and R_1 and θ are constants; θ is fixed by the requirement that the total amount of surfactant on the bubble equal $2\pi\chi$, whereas R_1 is chosen to remove the leading-order singularity in $\tau_p(v)$ at the cap edges, ensuring that the stress on the bubble is integrable. At the transition from mobile to stagnant surface (i.e. at the cap edges) there exists an $r^{1/2}$ singularity in Γ and $\boldsymbol{u}$ and an $r^{-1/2}$ singularity in the shear stress, where r is the distance from the cap edge (see Harper 1992 and Jensen & Halpern 1998 for related results).

Using the general method described in Siegel (1999), the exact steady solution is evaluated with the nonlinear equation of state. Figure 7 shows the $\beta > 0$ response curves for three representative values of β, and for $\epsilon = 0.01$. When the bubble is covered with surfactant, the resulting portion of the response curve is shown as a dashed line. The portion of the response curve corresponding to the surfactant cap solution is represented by a solid line. The most interesting feature of the $\beta > 0$ curves is the absence of the flat upper portion of the S-shaped curve seen when there is no surfactant. Instead the response curves terminate after a single turning point. Figures 8(*a*) and 8(*b*) depict the surfactant concentration and bubble profiles at the representative points *A*–*E* along the $\beta = 0.1$ response curve.

At the terminal point of the response curve (point *E*) a true cusped bubble is formed, i.e. the radius of curvature is zero at $v = 0, \pi$ (see figure 8*c*). At this point the surface tension also reaches zero, as is required to hold at a steady cusp (Pukhnachov 1973). Numerical evidence shows that the turning point corresponds to a change in stability for the steady solutions; the lower-branch solutions correspond to stable steady states whereas the upper-branch solutions are unstable. Thus for capillary numbers less than the value Q_c at a turning point, the time-dependent solution will evolve toward the proper rounded bubble steady state. For $Q > Q_c$ there is no longer

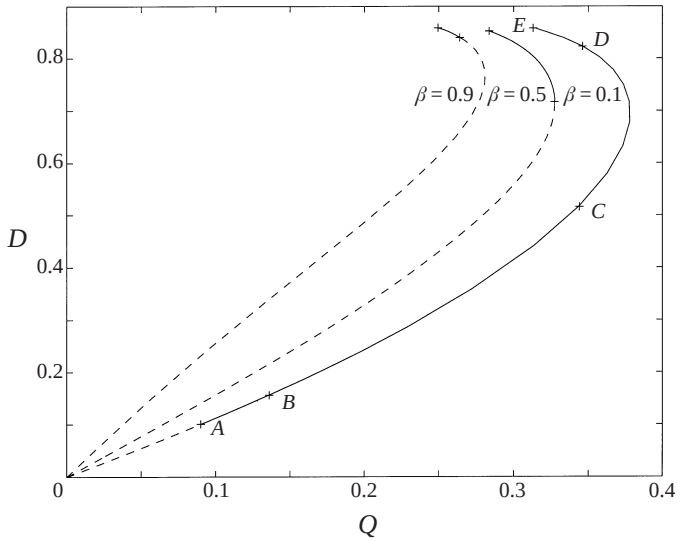

FIGURE 7. Response curves (deformation D versus capillary number Q) for $\beta = 0.1$, 0.5, and 0.9. Parameter values are $\epsilon = 0.01$, $Pe_s = \infty$ and $\chi = 0.5$. Dashed curves represent steady bubbles covered with a non-zero distribution of surfactant, while solid curves denote steady states with surfactant caps; the location of the transition point is denoted by a cross, as is the terminal point of each curve. Capital letters and accompanying crosses show the parameter values for the plots in figure 8.

a steady-state solution. These facts hint at a time-dependent evolution for $Q > Q_c$ in which the bubble continuously evolves until an unsteady cusped (i.e. infinite curvature) formation is achieved, much as in Taylor's experiment. Such a bubble can be viewed as a precursor to tip streaming. The surmised time-dependent behaviour is verified in § 5.5.

We comment on the role of the nonlinear equation of state. Roughly speaking, the exact steady solution for $Pe_s = \infty$ is independent of the functional form of the equation of state. Although this statement is not precisely true (the equation of state influences the cap angle θ through the normalization relation (14)), it does reflect the lack of any direct mention of $\Gamma(v)$ in (33). Thus, the main role of the equation of state is in deciding what surfactant distribution is necessary to obtain a given *surface tension distribution* satisfying (33). This consideration seems to limit the influence that differing equations of state can have on the properties of the steady solution. For example, consider an equation of state $\tau(\Gamma)$ which does not allow $\tau \to 0$. It might at first seem that this will preserve the existence of steady solutions for all Q, as well as the 'S' shape of the solution branch seen for constant surface tension (since $\tau \to 0$ is required in (31) to prevent $Q \to \infty$ as a cusped bubble is approached). However, after trying a number of $\tau(\Gamma)$ relations with τ bounded away from zero, we find in each case the steady solution branch terminates when the inversion of $\tau(\Gamma)$ to obtain $\Gamma(\tau)$ breaks down, at which point the surfactant cannot distribute itself in such a way as to obtain the τ required by the exact solution. Thus, the termination of the steady solution branch seems to be a generic feature when surfactant is present.

5.2. *Steady bubbles: $Pe_s < \infty$*

Numerical solutions for $Pe_s < \infty$ are considered in this section in order to examine the role of surface diffusion on the steady-state interfacial shape. In the case $Pe_s > 1$,

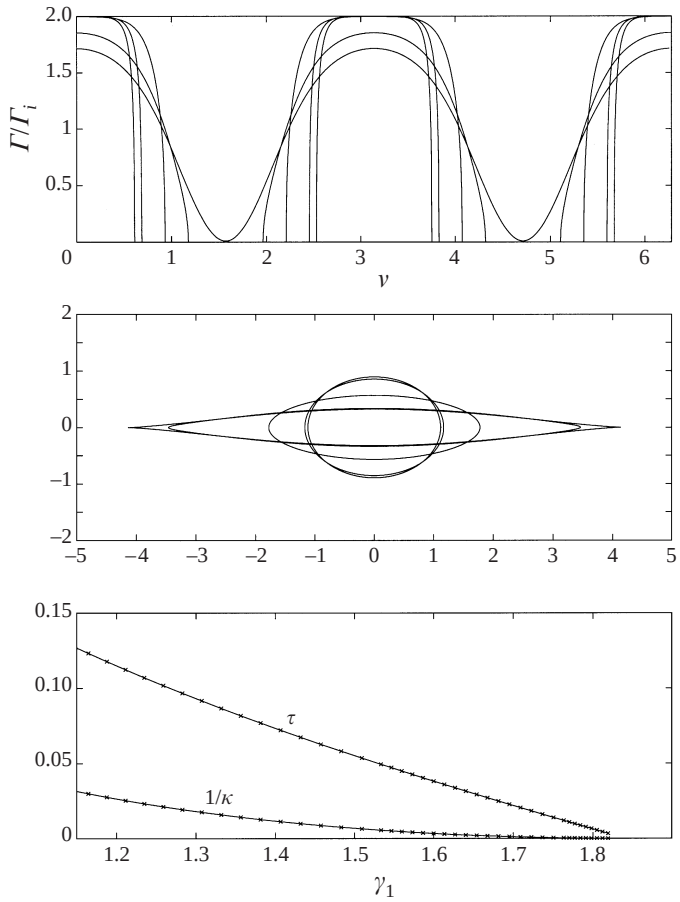

FIGURE 8. (*a*) Surfactant concentration Γ versus v, plotted at five representative points (marked *A*–*E*) along the $\beta = 0.1$ response curve (see figure 7). Surfactant caps are centred at $v = 0$ and $v = \pi$, with regions of zero surfactant concentration in between. (*b*) Bubble profiles at points marked *A*–*E* on the $\beta = 0.1$ response curve. (*c*) Radius of curvature $1/\kappa$ and non-dimensional surface tension τ at the points $v = 0$ and π, plotted at $\beta = 0.1$ and for a range of the map parameter γ_1 (used to characterize the deformation of the bubble). Note that the surface tension tends to zero at the point when a cusped bubble is formed.

the steady-state surfactant distribution associated with a given interface shape is determined using Newton iteration on (32). The basic algorithm is the same as that employed for rounded bubbles in Siegel (1999).

In contrast, it is found that a very large number of points is necessary to obtain an accurate solution for bubbles near cusping when Pe_s is small (i.e. $Pe_s \lesssim 1$). Newton's method, which involves the solution of an $N \times N$ matrix equation at each iteration, is prohibitively slow for N much greater than 1024. In this range, we have found that a simple method involving fixed-point iteration is more efficient. The fixed-point iteration scheme employed here takes the form (see (32))

$$\Gamma_v^{(k+1)} = \tfrac{1}{2} Pe_s |z_v|^2 \Gamma^{(k)} \mathscr{H}\left(\frac{\tau^{(k)}}{|z_v|}\right) - \epsilon Q Pe_s \Gamma^{(k)} |z_v|^2 \gamma_0^2 \sin 2v,$$

where $\Gamma^{(k)}$ denotes the kth iterate of $\Gamma(v)$ and $\tau^{(k)}$ is evaluated using $\Gamma^{(k)}$. Spectral

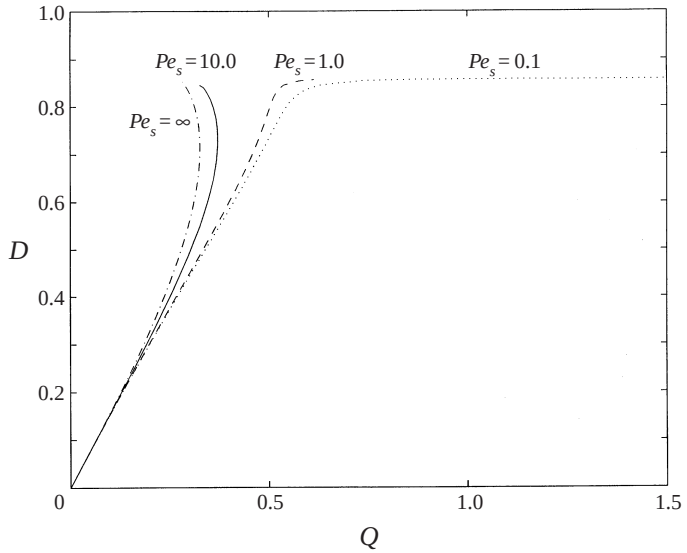

FIGURE 9. Response curves plotted for several values of Pe_s. Parameter values are $\epsilon = 0.01$, $\beta = 0.5$, and $\chi = 0.5$. The curve for $Pe_s = 0.1$ actually extends out to $Q = 2.419$ (not shown).

integration is employed to produce $\Gamma^{(k+1)}$. The constant of integration Γ_0 is determined from the normalization condition (14). This leads to

$$\Gamma_0 = \frac{2\pi\chi - \displaystyle\int_0^{2\pi} \Gamma_1(v')\,\mathrm{d}v'}{\displaystyle\int_0^{2\pi} |z_v|\mathrm{d}v'},$$

where $\Gamma_1(v) = \Gamma(v) - \Gamma_0$ is the periodic part of Γ. Although the convergence of the iterative scheme is linear, this algorithm requires only $O(N \ln N)$ operations per iteration, so that a very large number of points may be used. Up to $N = 8192$ points are used in the simulations reported here. For $Pe_s \lesssim 1$, the iteration converges even for bubble shapes that are very near cusped. The method does not converge for Pe_s much greater than one, so in that regime the scheme based on Newton's method is employed.

Figure 9 presents the response curves at $\beta = 0.5$ for several Pe_s values. At the terminal point of each curve the implemented iteration scheme no longer converges. However, it appears that the computed termination point lies near the actual termination point, where the bubble develops a true cusp and where the surface tension is zero at $v = 0, \pi$. This is supported by the curvature and surface tension trends as the terminal point is approached.

Figure 9 clearly shows that as surface diffusion increases, the response curve smoothly transforms from its form at $Pe_s = \infty$ to the form observed in the absence of surfactant. This behaviour might be expected, since the surfactant distribution is nearly constant when Pe_s is small and Q is not too large. In this condition the surface tension is nearly uniform along the bubble surface and surfactant merely reduces overall magnitude of surface tension from its clean flow value.

Similar behaviour is observed as the total amount of surfactant (as measured by χ) is decreased. Specifically, as χ is reduced with Pe_s held fixed, the response curve

again deforms toward the form exhibited in the absence of surfactant, much as in figure 9. The presence of non-zero diffusion appears to be important for this trend. In particular, when $Pe_s = \infty$ the upper, flat portion of the response curve is absent, regardless of the value of χ.

5.3. *Bubble with surfactant: transient evolution*

In this section the time-dependent behaviour of the interface is examined. Of particular interest are the details of the transient dynamics for small surface diffusion and for capillary numbers greater than the turning point value Q_c. The calculations are greatly simplified by exploiting the analytic structure of the $N = 1$ conformal map solution discussed in § 4. Doing so enables computations to be performed nearly up to cusp formation.

5.4. *Numerical method*

We start by presenting some preliminary calculations to transform the governing equations into a form convenient for numerical computation. First differentiate the area equation (29) to obtain an equation of the form $\dot{\gamma}_0 = q[\gamma_1]\dot{\gamma}_1$. Upon introducing the function $h(\gamma_1) = c_1 + ({c_1}^2 - c_2)$ and differentiating the relation (26) one obtains the expression

$$\dot{\gamma}_1 = \frac{\dot{\gamma}_2}{\epsilon[\gamma_0 + \gamma_1 s(\gamma_1)]}, \tag{35}$$

where

$$s(\gamma_1) = \frac{2\gamma_1 h - h'(1 + {\gamma_1}^2)}{[2h^3(1 + {\gamma_1}^2)]^{1/2}}$$

and $h' = \partial h/\partial\gamma_1$. Substitution of (28) into (35) leads to an expression for $\dot{\gamma}_1$ in terms of the other map parameters γ_i; given the surfactant distribution at time t, an explicit scheme is applied to this equation along with (26) and (29) to obtain the map parameters at time $t + \Delta t$.

To describe how the surfactant distribution $\Gamma(v, t)$ is updated, it is convenient to write equation (13) as

$$\frac{\partial\Gamma}{\partial t} + \Lambda_1(v, t)\Gamma_{vv} = F(\Gamma, \Gamma_v, t),$$

where $F(\Gamma, \Gamma_v, t)$ takes the form $F(\Gamma, \Gamma_v, t) = \Lambda_2(v, t)\Gamma_v + \Lambda_3(v, t)\Gamma$ and the coefficients $\Lambda_i(v, t), i = 1, \ldots, 3$, depend on the interface shape. Assuming that this shape is known at time $t + \Delta t$ and that $\Gamma(v, t)$ is known, then equation (13) is discretized as

$$\frac{\Gamma_j^{n+1} - \Gamma_j^n}{\Delta t} + \frac{\Lambda_1(v_j, t_n)}{2\Delta t}(\Gamma_{j+1}^{n+1} + \Gamma_{j-1}^{n+1} - 2\Gamma_j^{n+1}) = F(\Gamma_j^n, \Gamma_{vj}^n, t_n),$$

where we have introduced the notation $\Gamma_j^n = \Gamma(v_j, t_n)$ and where Γ_{vj}^n denotes the standard centred difference formula for Γ_v, centred at v_j. The resulting tridiagonal system can be inverted using standard techniques. Although this implicit Euler method is only first-order accurate in time, we have found this sufficient for our purposes. It is not difficult to adapt the method to achieve second-order accuracy. Computations for $Pe_s = \infty$ were performed with a straightforward explicit method, fourth-order accurate in time and pseudospectral in space. A useful check on the accuracy of either method is to monitor the total amount of surfactant, which must remain constant. The total amount of surfactant was found to change by 0.1–0.001% over the length of

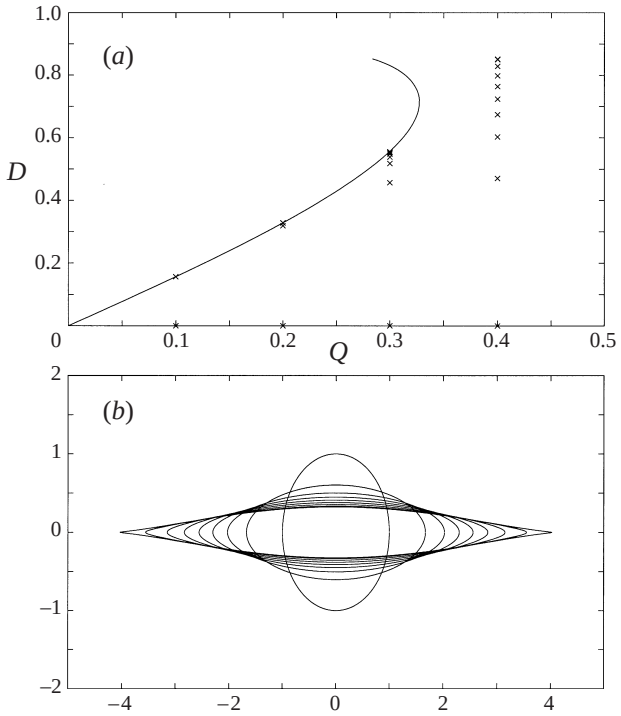

FIGURE 10. (*a*) Comparison of steady-state response curve with the computed transient evolution for various Q. Parameter values are $Pe_s = \infty$, $\beta = 0.5$, and $\chi = 0.5$. For each Q, the crosses represent the deformation of a time-evolving bubble starting from a circle ($D = 0$) at $t = 0$. The time increment between crosses is $\Delta t_m = 0.75$ for $Q = 0.1$, 0.2, 0.3 and $\Delta t_m = 0.5$ for $Q = 0.4$, with the final increment given by $\Delta t_m = 0.45$. For $Q = 0.1$, 0.2, and 0.3 the time-dependent evolution approaches a steady state, whereas for $Q = 0.4$ the bubble evolves without limit until an unsteady cusped formation is reached. (*b*) Bubble profiles for the time-dependent evolution shown in (*a*), in the case $Q = 0.4$.

a calculation, depending on the time and space intervals and the method used. Thus, there was no need to renormalize the surfactant concentration periodically throughout the calculation as has often been found necessary to prevent degradation of accuracy (see e.g. Stone & Leal 1990). For all the results reported in the next section, it was checked that decreasing the time step or the space interval did not affect the results. As a means of verification, it was checked that the transient calculations gave results in complete agreement with the exact steady-state solutions exhibited in the previous section.

5.5. *Transient behaviour, numerical results*

A comparison of the steady-state response curve with the results of transient calculations for several values of the capillary number Q is shown in figure 10. The parameter values are $\beta = 0.5, \chi = 0.5$, and $Pe_s = \infty$. The crosses for fixed Q depict the deformation of a time-evolving bubble starting from a circle with $D = 0$ at $t = 0$. Note that for $Q < Q_c$ the crosses indicate that a steady bubble solution is quickly reached, and the steady deformation is in precise agreement with the exact steady solution of the previous section (denoted by a solid curve). In contrast, initial shapes and surfactant distributions that are 'near' a steady solution on the upper branch of the response curve did not evolve back to a steady shape. Hence, the upper portion

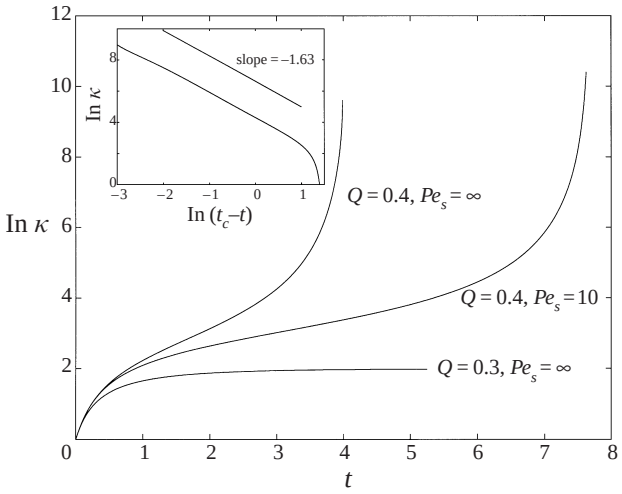

FIGURE 11. Plot of $\ln \kappa$ versus time for the unsteady calculations of figure 10, in the cases $Q = 0.3$ and $Q = 0.4$. For $Q = 0.3$ the evolution approaches a steady state, whereas for $Q = 0.4$ it exhibits rapid growth indicative of singularity formation. Rapid growth is also observed for $Q = 0.4$ and $Pe_s = 10$ (weak diffusion). Inset: the approach to the singularity in the case $Q = 0.4, Pe_s = \infty$ is described by the functional form $\kappa \sim c(t_c - t)^{-1.63}$, where $t_c = 4.03$ is the estimated critical time.

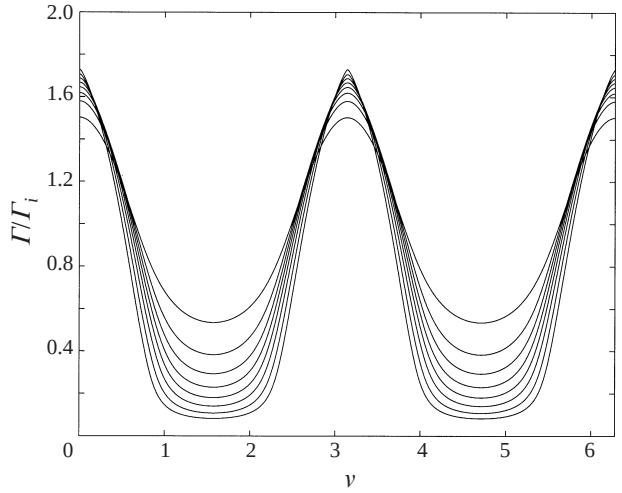

FIGURE 12. Surfactant concentration for the unsteady calculation of figure 10, in the case $Q = 0.4$, $Pe_s = \infty$. The curves are shown for $t = 0.5$ to 3.95 with the time increments given in figure 10.

of each response curve is a branch of unstable solutions. When $Q > Q_c$ there is no allowable steady-state solution. Thus, the bubble evolves without limit. Only a couple of outcomes are consistent with the form (25) of the conformal map and conditions (26), (29). One is that the bubble oscillates indefinitely, i.e. a limit cycle is approached. The other is that an unsteady cusped formation is achieved. Our numerical evidence for $Q = 0.4 > Q_c$ suggests that the latter outcome comes to pass.

The transient bubble profiles for $Q = 0.4$ are displayed in figure 10(b). A plot of $\ln \kappa$ versus time (figure 11), where κ is the tip curvature, provides strong evidence that a true cusp singularity is realized in finite time, despite positive surface tension over

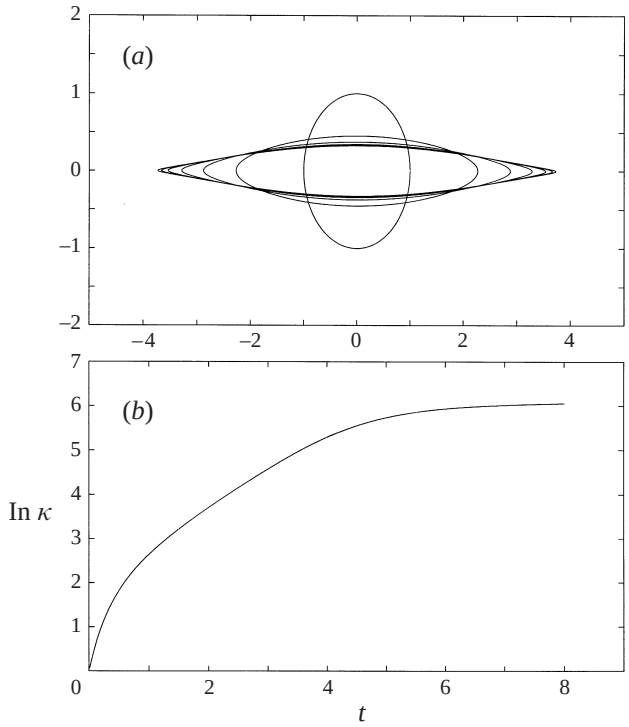

FIGURE 13. (*a*) Bubble profiles for transient evolution with parameter values $Pe_s = 0.1$, $\beta = 0.5$, $\chi = 0.5$, and $Q = 0.6$. The time interval between successive profiles is $\Delta t_p = 1.0$. (*b*) Plot of $\ln\kappa$ versus time for the parameter values in (*a*). The evolution approaches a steady state.

the entire surface. The figure demonstrates that the blow-up for $Pe_s = \infty$ exhibits the functional form $\kappa \sim c_1(t_c - t)^{-1.63}$ where $t_c = 4.03$ is the estimated critical time, and the numerical uncertainty in the exponent is estimated to be ± 0.05. As shown by figure 12, the need to resolve a rapid change in the slope of Γ at the equator (this behaviour is absent in the steady solutions) limits how close we can get to t_c. This in turn limits the number of decades of scaling behaviour exhibited in figure 11. Similar blow-up is observed for sufficiently large but finite Pe_s (i.e. weak surfactant diffusion), since the response curve has the same form as for $Pe_s = \infty$ (see figure 11). For comparison, the log-curvature is also plotted using the parameter values $Q = 0.3$, $Pe_s = \infty$, for which the evolution approaches a steady state.

Finally, the effect of increasing surface diffusion is illustrated in figure 13. Here the time-dependent interface profiles and curvature are shown for parameter values $Q = 0.6$ and $Pe_s = 0.1$. As expected, the evolution approaches a steady state, despite a value of Q that is considerably higher than that which led to unsteady cusped bubbles for $Pe_s \gg 1$.

In summary, the numerical results provide strong evidence that a true cusp singularity occurs in finite time for a bubble evolving in an Antanovskii-type straining flow with variable surface tension. The singularity is avoided in the case of constant surface tension. The formation of an unsteady cusped bubble at a critical value of capillary number Q is viewed as the onset to tip streaming.

Pozrikidis also considers the transient evolution with surfactant. His results are for the most part consistent with the present work. For example, when $\epsilon = 0.05$, $\beta = 0.5$,

χ^{-1}	Q_c
2.0	0.39
3.0	0.41
5.0	0.45
7.0	0.47

TABLE 1. Location of the turning point Q_c for $\beta = 0.1$, $Pe_s = \infty$, as a function of the initial amount of surfactant χ.

$Q = 0.6$ and $Pe_s = 20$ or 200 the computations in Pozrikidis (1998) show that the bubble evolves toward an unsteady cusped shape much like that shown in figures 10 and 11. However, the numerics breaks down before the curvature gets too large, and evidence of growth of curvature is not as strong as in the present work. The results do differ somewhat from those presented here in the case $\beta = 0.2$, $Pe_s = 20$. For these parameter values, the bubble is observed to evolve toward a cusped shape as in the previous example, but instead of achieving a true cusp (as occurs for the exact mathematical solution of the form (25)) the curvature saturates and narrow jets stream out from the bubble tips. The difference with our result is probably due to the sensitivity of the evolution near highly cusped interfaces, as described earlier.

6. Discussion

Despite the drastic simplifications employed in our analysis, it is interesting to compare the theoretically predicted Q_c, at which the bubble makes a transition from a steady rounded configuration to the unsteady cusp-like formation, to the values obtained in Taylor's experiment. There are three remaining parameters, β, χ, and Pe_s, that need to be determined from the experimental conditions. Although this cannot be precisely done for the fluids employed by Taylor† the parameter values can be estimated using representative values for the physical constants. The modified surface Péclet number typically satisfies $Pe_s \gg 1$ and is set to infinity. A representative range of values for the surface tension σ_0 at a clean interface in an oil–water combination at room temperature is 25–50 dyn cm^{-1}. A typical value for the product $RT\Gamma_\infty$ is 5 dyn cm^{-1} at room temperature (the maximum packing density Γ_∞ does not vary greatly among fluid combinations) (Charles Malderelli, private communication). This gives a value for $\beta = RT\Gamma_\infty/\sigma_0$ in the range 0.1–0.2. Since there is no obvious characteristic value for χ, we will present values of the critical capillary number for a range of this parameter.

Table 1 presents the calculated value of the critical capillary number for $\beta = 0.1$, $\epsilon = 0.01$ and a range of χ. The calculated values of Q_c are not very sensitive to the value of χ, and they compare favourably with the experimentally observed value $Q_c = 0.41$. For smaller bubbles with ϵ less than 0.004 the $\beta = 0$ response curve has two turning points, with the first turning point associated with a sudden transition from a steady rounded to a steady cusped bubble. However, the values of ϵ and Q_c required for this to happen, namely $\epsilon < 0.004$ and $Q_c = 0.61$, do not match the experimental values at the first transition, given by $\epsilon = 0.01$ and $Q_c = 0.41$. Instead,

† Taylor (1934) filled the four-roller mill with 'golden syrup', which is a concentrated sugar solution. A mixture of carbon tetrachloride and paraffin oil was utilized for the drop phase to obtain the lowest viscosity ratio $\mu_{drop}/\mu_{liquid} = 0.0003$.

they are consistent with the parameter values at the second transition observed by Taylor, occurring at $Q = 0.65$ and $\epsilon = 0.0025$, in which a steady rounded bubble suddenly transforms to a steady cusp-like bubble. Thus, the two-dimensional model gives results that are consistent with experimental observation, if we use the $\beta > 0$ model with $\epsilon = 0.01$ to describe the first transition and the $\beta = 0$ model with $\epsilon < 0.004$ to describe the second one. Justification for using the two different models follows from the supposition that surfactant is removed from the bubble during tip streaming, and that the bubble remaining after tip streaming is smaller in size. The match between theory and experiment may indicate that the simplified model employed here still incorporates much of the relevant physics.

7. Conclusion

We have considered the transient evolution of an inviscid bubble in a two-dimensional model of Taylor's four-roller mill. For bubbles evolving under constant surface tension with $\epsilon > 0.004$ (so that the curve $D(Q)$ is monotonic), it is found that a previously determined steady solution branch is linearly stable for all capillary numbers, although the bubble is unstable to certain finite-amplitude perturbations. This answers negatively a conjecture concerning the possible existence of a critical capillary number for linear instability. The evolution at zero surface tension is found to lead to unsteady finite-time cusp formation. A general theory of time-dependent evolution, which includes the existence of a broad class of exact solutions, is also presented. The theory holds for constant as well as variable surface tension.

We have also considered the effect of variable surface tension, caused by the presence of surfactant, on the steady-state shape and time-dependent evolution. At issue is the possible spontaneous occurrence of singularities on the bubble surface, which may be viewed as a precursor to tip streaming. The form of the steady-state solution branches and known analytic structure of the time-dependent solution is highly suggestive of spontaneous singularity formation in the time-dependent evolution for $Q > Q_c$. Actual finite-time singularity formation in the transient evolution is verified through numerical calculation. The numerical calculations are greatly simplified by the analytic structure of the conformal map solution. Analogous behaviour is observed for finite Pe_s.

If the formation of finite-time cusp singularities is interpreted as a precursor to tip streaming, then the surfactant-induced transition from steady to unsteady cusped bubble provides a mechanism for bubble breakup at small capillary numbers, as is observed in experiment. In contrast, the interfacial pinching observed at constant surface tension only occurs at larger values of Q. It is not clear whether the general tendencies uncovered here carry over to three-dimensional flow. Numerical calculations for axisymmetric bubbles and far-field conditions (i.e. the axisymmetric counterpart of (4)) show behaviour remarkably similar to that for two-dimensional bubbles. Steady nearly cusped interfacial shapes were computed for $\epsilon = 0$ by Youngren & Acrivos (1976), and for other values of ϵ by Pozrikidis (1998). For $\epsilon \geqslant 0$ the computed steady (clean bubble) solution branches terminate due to resolution difficulties at the highly curved tips; however slender body theory (Buckmaster 1972; Sherwood 1984) suggests that the steady solutions exist for arbitrarily large Q, much as for two-dimensional clean bubbles. The stability of these solutions has not been ascertained, although the indications from transient calculations (Pozrikidis 1998) and slender body theory are that the shapes are unstable above a critical capillary number. Numerical calculations for axisymetric bubbles probably suffer from the same sensitivity to small

finite-amplitude disturbances at large Q detailed in § 3, so care must be excercised in their use. As for two dimensions, simulations show that the presence of surfactant tends to promote cusp formation and tip streaming at capillary numbers for which the constant surface tension bubble approaches a steady state (Milliken *et al.* 1993; Pozrikidis 1998).

Also neglected in our solutions is the flow inside the bubble, since the viscosity of the inner fluid is assumed negligible. Interior viscous stresses provide an alternative mechanism for breakup. The scaling (Acrivos & Lo 1978; Hinch & Acrivos 1979) $Q_c \sim \lambda^{-1/6}$ where λ is the viscosity ratio suggests that λ must be very small for surfactant effects to be the dominant mechanism for breakup. Other factors not considered in these studies, such as diffusion and/or transport of surfactant from the interface to the bulk fluid, may also influence the formation of cusped solutions. This needs to be considered in future work.

Appendix A

We describe the numerical method used to investigate linear stability of the steady solutions, and the method used to solve for the time-dependent evolution for general interface shapes. A form of the governing equation for a general mapping function $z(\zeta, t)$ on $|\zeta| = 1$ (without surfactant) that is convenient for numerical computation has been given by Antanovskii (1994*b*). In terms of the dimensionless variables defined in § 2.1, the equation takes the form

$$2\,\mathrm{Im}\,\{z_t\overline{\mathrm{i}\zeta z_\zeta}\} = K(U_0 + \bar{z}U_1) + K(\bar{z}z_t), \tag{A 1}$$

where

$$U_0 = -z^2 \quad \text{and} \quad U_1 = -\zeta z_\zeta \left\{ \frac{1}{Q|z_\zeta|} - \mathrm{Re}\left[\frac{\epsilon z^3}{\zeta z_\zeta}\right] + \mathscr{H}\left(\frac{1}{Q|z_\zeta|} - \mathrm{Re}\left[\frac{\epsilon z^3}{\zeta z_\zeta}\right]\right)\right\}. \tag{A 2}$$

Here $\mathscr{H}$ is the Hilbert transform and the operator K is defined by

$$K(f) = \frac{\partial}{\partial v}\,\mathrm{Im}\,\{f(v,t) - \mathscr{H}[f(v,t)]\}.$$

The linearized evolution equation for the perturbation $\tilde{z}$ defined in (15) is obtained in the standard way. The general power series representation (16) is truncated at $j = N-2$, substituted into the linearized evolution equation, and the resulting equation is evaluated at N points $\zeta_k = \mathrm{e}^{\mathrm{i}kh}$ on the upper half-semi-circle, where $h = \pi/(N-1)$ and $k = 0, \ldots, N-1$. This leads to a linear system of ordinary differential equations of the form $\boldsymbol{A}\boldsymbol{X}_t = \boldsymbol{B}\boldsymbol{X}$ where $\boldsymbol{A}$ and $\boldsymbol{B}$ are $N \times N$ matrices and $\boldsymbol{X}^T = (\hat{a}_{-1}, \ldots, \hat{a}_{N-2})$. These matrices have the specific form

$$A_{ij} = [2\,\mathrm{Im}\,(\overline{\mathrm{i}\zeta z_{s\zeta}}\zeta^j) - K(\bar{z}_s\zeta^j)] \quad (\zeta = \zeta_i),$$

$$B_{ij} = K[U_{0j} + \bar{z}_s U_{1j} + U_1(z_s)\zeta^{-j}] \quad (\zeta = \zeta_i),$$

where

$$U_{0j} = -2z_s\zeta^j,$$

$$U_{1j} = -\zeta z_{s\zeta}[f_1 + \mathscr{H}(f_1) - j\zeta^j(f_2 + \mathscr{H}(f_2))] - 3\epsilon z_s^2\zeta^j,$$

with

$$f_1 = -\frac{1}{Q|z_{s\zeta}|}\,\mathrm{Re}\left[\frac{j\zeta^j}{\zeta z_{s\zeta}}\right] + \mathrm{Re}\left[\frac{\epsilon z_s^3}{\zeta z_{s\zeta}}\left(\frac{j\zeta^j}{\zeta z_{s\zeta}} - \frac{3\zeta^j}{z_s}\right)\right],$$

$$f_2 = \frac{1}{Q|z_{s\zeta}|} - \mathrm{Re}\left[\frac{\epsilon z_s^3}{\zeta z_{s\zeta}}\right]$$

for $i, j = -1, \ldots, N-2$. Taking advantage of the non-singularity of $\boldsymbol{A}$, we reduce the problem to a standard eigenvalue problem $\boldsymbol{A}^{-1}\boldsymbol{B}\boldsymbol{X} = \sigma\boldsymbol{X}$, which is solved by the software package LAPACK. In practice we have found it convenient to separately treat symmetric perturbations where $\tilde{z}$ contains only odd powers of ζ and antisymmetric perturbations consisting of even powers of ζ. Additionally, a dealiasing procedure analogous to that described below was found to improve the accuracy of computations for highly cusped bubbles.

The method used to investigate the time-dependent evolution for general interface shapes is also described. Represent z and $\partial z/\partial t = u$ by truncated Laurent expansions

$$z(\zeta, t) = \sum_{m=-1}^{N-2} z_m(t)\zeta^m, \qquad u(\zeta, t) = \sum_{m=-1}^{N-2} u_m(t)\zeta^m,$$

with $z^{-1} > 0$ and $\mathrm{Im}\,(u_{-1}) = 0$. The discrete version of (36) becomes (Antanovskii 1994*b*)

$$\sum_{m=k-1}^{N-2} (m-k)u_m\bar{z}_{m-k} + \sum_{m=-1}^{N-2-k} m\bar{u}_m z_{m+k} = k\bar{\hat{U}}_{-k}, \quad k = 0, \ldots, N-1, \tag{A 3}$$

where $\hat{U}_{-k}$ is the coefficient of ζ^{-k} in the Laurent expansion of $U_1(\zeta, t)$. Since the equation for $k = 0$ is real, the system is supplemented by the relation $\mathrm{Im}\,u_{-1} = 0$ to give $2N$ equations for the $2N$ unknowns $\mathrm{Re}\,u_m$, $\mathrm{Im}\,u_m$, $m = -1, \ldots, N-2$. Given $z(\zeta, t)$ the coefficients z_m are obtained from the discrete Fourier transform (DFT). Likewise, the operators $\mathscr{H}$, K, and the coefficients $\hat{U}_{-k}$ are evaluated using the DFT. The linear system (38) can then be solved directly or by employing an iterative technique. We use the generalized minimum residual method GMRES. The coefficients z_k are then updated through the relation

$$\frac{\partial z_k}{\partial t} = u_k$$

using a fourth-order Adams–Moulton solver.

In practice, aliasing errors caused by truncation of the system contaminate the numerical calculation. We therefore perform dealiasing in the calculation by padding the Fourier representation of z with N modes of zero amplitude, thereby computing the quantities U_0 and U_1 with $2N$ points. With dealiasing, we do not find it necessary to greatly increase N when the curvature of the bubble ends is large, as is suggested in Antanovskii (1994*b*).† In some cases we also employ a spectral filter (see e.g. Krasny 1986) to prevent round-off error in the large-k modes from growing and adulterating the computations. In the filtering procedure, all Fourier modes satisfying $|z_k| < \delta$ are set to zero. A typical value of δ is 10^{-12}.

† Although some terms in the bracketed expression in (A 2) have singularities at $\pm\zeta_0$ and $\pm 1/\zeta_0$, where ζ_0 is a zero of z_ζ, the singularity at $1/\zeta_0$ is removed by projection onto + wavenumber space during the formation of U_1 and the singularity at ζ_0 is removed by the projection onto − wavenumber space during the formation of K.

Appendix B

We derive a simplified expression for $I(\gamma_2^{1/2}, t)$ which is used in (28). Upon performing the expansion

$$\frac{1}{\zeta'}\left[\frac{\zeta' + \gamma_2^{1/2}}{\zeta' - \gamma_2^{1/2}}\right] = \frac{1}{\zeta'} + 2\sum_{n=1}^{\infty} \frac{\gamma_2^{n/2}}{\zeta'^{n+1}},$$

which holds for $\gamma_2 < 1$, it is easy to see that

$$\frac{1}{2\pi \mathrm{i}} \oint_{|\zeta|=1} \mathrm{Re}\left[\frac{\epsilon\gamma_0^2}{\zeta'^2}\right] = \epsilon\gamma_0^2\gamma_2.$$

It follows that

$$I(\gamma_2^{1/2}, t) = \frac{\epsilon\gamma_0^2}{\gamma_2} - \left[\epsilon\gamma_0^2 \frac{1-\gamma_2^2}{\gamma_2} - \frac{1}{2\pi \mathrm{i} Q} \oint_{|\zeta|=1} \frac{\tau}{|z_\zeta|}\right].$$

Some tedious but straightforward algebra can then be performed to obtain the identity

$$\frac{\tau}{|z(\zeta)|}\frac{\zeta' + \gamma_2^{1/2}}{\zeta' - \gamma_2^{1/2}} = \tau \frac{1 - \gamma_2^2 + \gamma_2/\zeta'^2 + 2\gamma_2^{1/2}/\zeta' - \gamma_2\zeta'^2 - 2\gamma_2^{3/2}\zeta'}{|\gamma_0(1 - 3\gamma_2\zeta^2) - \gamma_1\zeta^2(1 + \gamma_2\zeta^2)|}.$$

Symmetry arguments can be employed to show that only the first two (i.e. constant) terms in the numerator of the above expression remain after integration over the unit circle. As a result

$$I(\gamma_2^{1/2}, t) = \frac{\epsilon\gamma_0^2}{\gamma_2} - \left[\epsilon\gamma_0^2 \frac{1-\gamma_2^2}{\gamma_2} - \frac{1-\gamma_2^2}{2\pi Q} \int_0^{2\pi} \frac{\tau(v', t)}{|\gamma_0(1 - 3\gamma_2\zeta^2) - \gamma_1\zeta^2(1 + \gamma_2\zeta^2)|}\, \mathrm{d}v'\right]$$

which is the desired equation.

REFERENCES

Acrivos, A. & Lo, T. S. 1978 Deformation and breakup of a single slender drop in an extensional flow. *J. Fluid Mech.* **86**, 641–672.

Antanovskii, L. K. 1994*a* Influence of surfactants on a creeping free-boundary flow induced by two counter-rotating horizontal thin cylinders. *Eur. J. Mech.* B/*Fluids* **13**, 73–92.

Antanovskii, L. K. 1994*b* A plane inviscid incompressible bubble placed within a creeping viscous flow: Formation of a cusped bubble. *Eur. J. Mech.* B/*Fluids* **13**, 491–509.

Antanovskii, L. K. 1994*c* Quasi-steady deformation of a two-dimensional bubble placed within a potential flow. *Meccanica-J. Ital. Assoc. Teor. Appl. Mech.* **29**, 27–42.

Antanovskii, L. K. 1996 Formation of a pointed drop in Taylor's four-roller mill. *J. Fluid Mech.* **327**, 325–341.

Bentley, B. J. & Leal, L. G. 1986 An experimental investigation of drop deformation and breakup in steady, two-dimensional linear flows. *J. Fluid Mech.* **167**, 241–283.

Bruijn, R. A. de 1993 Tipstreaming of drops in simple shear flows. *Chem. Engng Sci.* **48**, 277–284.

Buckmaster, J. D. 1972 Pointed bubbles in slow viscous flow. *J. Fluid Mech.* **55**, 385–400.

Buckmaster, J. D. & Flaherty, J. E. 1973 The bursting of two-dimensional drops in slow viscous flow. *J. Fluid Mech.* **60**, 625–639.

Ceniceros, H. & Hou, T. 2000 The singular perturbation of surface tension in Hele-Shaw flows. *J. Fluid Mech.* **409**, 251–272.

Edwards, D. A., Brenner, H. & Wasan, D. T. 1991 *Interfacial Transport Processes and Rheology*. Butterworth-Heinemann.

Grace, H. P. 1982 Dispersion phenomena in high viscosity immiscible fluid systems and application of static mixers as dispersion devices in such systems. *Chem. Engng Commun.* **14**, 225–277.

Harper, J. F. 1992 The leading edge of an oil slick, soap film, or bubble stagnant cap in Stokes flow. *J. Fluid Mech.* **237**, 23–32.

Hinch, E. J. & Acrivos, A. 1979 Steady long slender droplets in two-dimensional straining motion. *J. Fluid Mech.* **91**, 401–414.

Hopper, R. W. 1990 Plane Stokes flow driven by capillarity on a free surface. *J. Fluid Mech.* **213**, 349–375.

Hopper, R. W. 1991 Plane Stokes flow driven by capillarity on a free surface. Part 2. Further developments. *J. Fluid Mech.* **230**, 355–364.

Howison, S. D. & Richardson, S. 1995 Cusp development in free boundaries, and two-dimensional slow viscous flows. *Eur. J. Appl. Maths* **6**, 441–454.

Jensen, O. E. & Halpern, D. 1998 The stress singularity in surfactant-driven thin-film flows. Part 1. Viscous effects. *J. Fluid Mech.* **372**, 273–300.

Jeong, J. T. & Moffatt, H. K. 1992 Free surface cusps associated with flow at low Reynolds number. *J. Fluid Mech.* **241**, 1–22.

Joseph, D. D. 1992 Understanding cusped interfaces. *J. Non-Newtonian Fluid Mech.* **44**, 127–148.

Joseph, D. D., Nelson, J., Renardy, M. & Renardy, Y. 1991 Two-dimensional cusped interfaces. *J. Fluid Mech.* **223**, 383–409.

Krasny, R. 1986 On singularity formation in a vortex sheet and the point vortex approximation. *J. Fluid Mech.* **167**, 65–93.

Mikhlin, S. G. 1957 *Integral Equations*. Pergamon.

Milliken, W. J., Stone, H. A. & Leal, L. G. 1993 The effect of surfactant on transient motion of Newtonian drops. *Phys. Fluids* A **5**, 69–79.

Muskhelishvili, N. I. 1953 *Singular Integral Equations*. P. Noordhoff.

Pozrikidis, C. 1997 Numerical studies of singularity formation at free surfaces and fluid interfaces in two-dimensional Stokes flow. *J. Fluid Mech.* **331**, 145–167.

Pozrikidis, C. 1998 Numerical studies of cusp formation at fluid interfaces in Stokes flow. *J. Fluid Mech.* **357**, 29–57.

Pukhnachov, V. V. 1973 On smoothness of the steady-state solutions of the Navier–Stokes equations near the free boundary. *Dinamika Sploshnoi Sredy* **15**, 133–144.

Richardson, S. 1968 Two-dimensional bubbles in slow-viscous flow. *J. Fluid Mech.* **33**, 475–493.

Richardson, S. 1973 Two-dimensional bubbles in slow-viscous flow. Part 2. *J. Fluid Mech.* **58**, 115–127.

Richardson, S. 1992 Two-dimensional slow-viscous flows with time-dependent free boundaries driven by surface tension. *Eur. J. Appl. Maths* **3**, 193–207.

Richardson, S. 1997 Two-dimensional stokes flows with time-dependent free boundaries driven by surface tension. *Eur. J. Appl. Maths* **8**, 311–329.

Sherwood, J. D. 1984 Tip streaming from slender drops in a nonlinear extensional flow. *J. Fluid Mech.* **144**, 281–295.

Siegel, M. 1999 Influence of surfactant on rounded and pointed bubbles in two-dimensional Stokes flow. *SIAM J. Appl. Maths* **59**, 1998–2027.

Stone, H. A. & Leal, L. G. 1990 The effects of surfactants on drop deformation and breakup. *J. Fluid Mech.* **222**, 161–186.

Tanveer, S. & Vasconcelos, G. L. 1995 Time-evolving bubbles in two-dimensional Stokes flow. *J. Fluid Mech.* **301**, 325–344.

Taylor, G. I. 1934 The formation of emulsions in definable fields of flow. *Proc. R. Soc. Lond.* A **146**, 501–523.

Torza, S., Cox, R. G. & Mason, S. G. 1972 Particle motions in sheared suspensions XXVII. Transient and steady deformation and burst of liquid drops. *J. Colloid Interface Sci.* **38**, 395–411.

Wong, H., Rumschitzki, D. & Maldarelli, C. 1996 On the surfactant mass balance at a deforming fluid interface. *Phys. Fluids* A **8**, 3203–3204.

Youngren, G. K. & Acrivos, A. 1976 On the shape of a gas bubble in a viscous extensional flow. *J. Fluid Mech.* **76**, 433–442.